

Dating of the NorthGRIP Ice Core by Inversion of a  
Simple Flow Model

Master Thesis by

Susanne Lilja Buchardt

Supervisor: Dorte Dahl-Jensen

Department of Geophysics  
Niels Bohr Institute  
Denmark

2005

# Abstract

In 2003 bedrock was reached at the NorthGRIP drill site, located at 75.12°N, 42.32°W. The recovered ice core contains an unbroken climate record reaching back to the Eemian warm period [North Greenland Ice Core Project Members, 2004]. In this thesis a new timescale for the ice core is derived using a two-dimensional flow model. The flow of the ice in the vicinity of the drill site is simulated with a modified Dansgaard-Johnsen model. Several unknown input parameters are estimated through a Monte Carlo inversion of the flow model. Observed internal radio-echo horizons in the ice are used to constrain this inversion. The derived timescale assigns an age of 126,500 years to the bottom of the ice at NorthGRIP. This ice is estimated to have been deposited 48 km upstream from the drill site. The inversion of the model reveals changing melt rates along the flow line leading to the NorthGRIP drill site. The melt rate at the NorthGRIP site is estimated to  $4.1 \pm 0.5$  mm/yr, which is the lowest value revealed in the area studied in this thesis.

# Contents

<b>1</b>	<b>Introduction</b>	<b>1</b>
<b>2</b>	<b>Background</b>	<b>5</b>
2.1	A Short Introduction to Glaciology . . . . .	5
2.1.1	Densification . . . . .	5
2.1.2	Temperatures . . . . .	6
2.1.3	$\delta^{18}\text{O}$ . . . . .	7
2.1.4	Ice Crystal Structure . . . . .	7
2.1.5	Deformation of Ice . . . . .	8
2.1.6	Ice Flow . . . . .	10
2.2	Internal Layers in Ice . . . . .	10
2.2.1	The Basic Equations . . . . .	11
2.2.2	The Cause of Increased Reflection . . . . .	12
2.2.3	Interpretation of the Layers . . . . .	12
<b>3</b>	<b>Modelling the Ice Flow</b>	<b>14</b>
3.1	The Flow in the NorthGRIP Area . . . . .	14
3.2	The Flow Model . . . . .	14
3.3	The Accumulation Model . . . . .	18
3.4	Computational Approach . . . . .	20
<b>4</b>	<b>Monte Carlo Inversion Theory</b>	<b>22</b>
4.1	Inverse Problems . . . . .	22
4.2	Introducing Probability Densities . . . . .	23
4.3	The Likelihood Function . . . . .	25
4.4	The Inverse Monte Carlo Algorithm . . . . .	26
<b>5</b>	<b>The Observed Data</b>	<b>28</b>
<b>6</b>	<b>Inversion of the Flow Model</b>	<b>32</b>
6.1	A Priori Information . . . . .	32
6.2	Choosing the Fix Points . . . . .	33

---

6.3	Accounting for Uncertainties . . . . .	34
6.4	Creating the Random Walk . . . . .	35
<b>7</b>	<b>Results and Discussion</b>	<b>38</b>
7.1	The Model Parameters . . . . .	38
7.1.1	The Basal Melt Rate, $w_b$ . . . . .	38
7.1.2	The Kink Height, $h$ . . . . .	42
7.1.3	The Fraction of Basal Sliding, $F_B$ . . . . .	42
7.1.4	The Accumulation History . . . . .	44
7.2	Correlation Between the Parameters . . . . .	45
7.3	The New Timescale . . . . .	45
7.4	Discussion of Assumptions . . . . .	49
7.5	Comparison With Observations . . . . .	50
7.6	The One-Dimensional Model . . . . .	50
<b>8</b>	<b>Conclusion</b>	<b>53</b>
<b>9</b>	<b>Outlook</b>	<b>55</b>

# Chapter 1

## Introduction

The Greenland Ice Sheet constitutes a unique high resolution archive of climate information. A snow layer deposited on the surface in a given year is subsequently buried by the snow falling during the following years. As the layer sinks down it is slowly compressed to ice, and except for postdepositional smoothing by diffusional processes, its chemical and isotopic compositions are preserved. The isotopic composition contains information on the atmospheric temperature at the time of condensation [Dansgaard, 1964], and on the source region of the precipitation [Johnsen et al., 1989]. Dust content, acidity, and the concentrations of various ions give information about storminess, volcanic eruptions, and the chemical composition of the atmosphere, respectively. Furthermore, the ice contains small bubbles of air that serve as sealed samples of past atmospheres. Thus the study of ice cores recovered from the ice sheet provide valuable information on the past climate of the Earth.

The first time bedrock was reached at an ice core drill site in Greenland was in 1966 at Camp Century in Northern Greenland. Since then, several deep ice cores have been drilled through the ice sheet. Fig. 1.1 shows the location of six drill sites in Greenland where climate records reaching far back in time have been obtained. This thesis deals with the dating of the ice core from NorthGRIP.

The background for the NorthGRIP project began with the drilling of the GRIP and GISP2 ice cores in Central Greenland in the early nineties. Because these two cores were drilled only 28 km apart, they were expected to contain similar climatic information. This held good in the upper 90 % of the cores, but below that their climate records began to differ significantly. It was later concluded that layers older than 105,000 years were disturbed by folding caused by the ice flowing over the relatively uneven

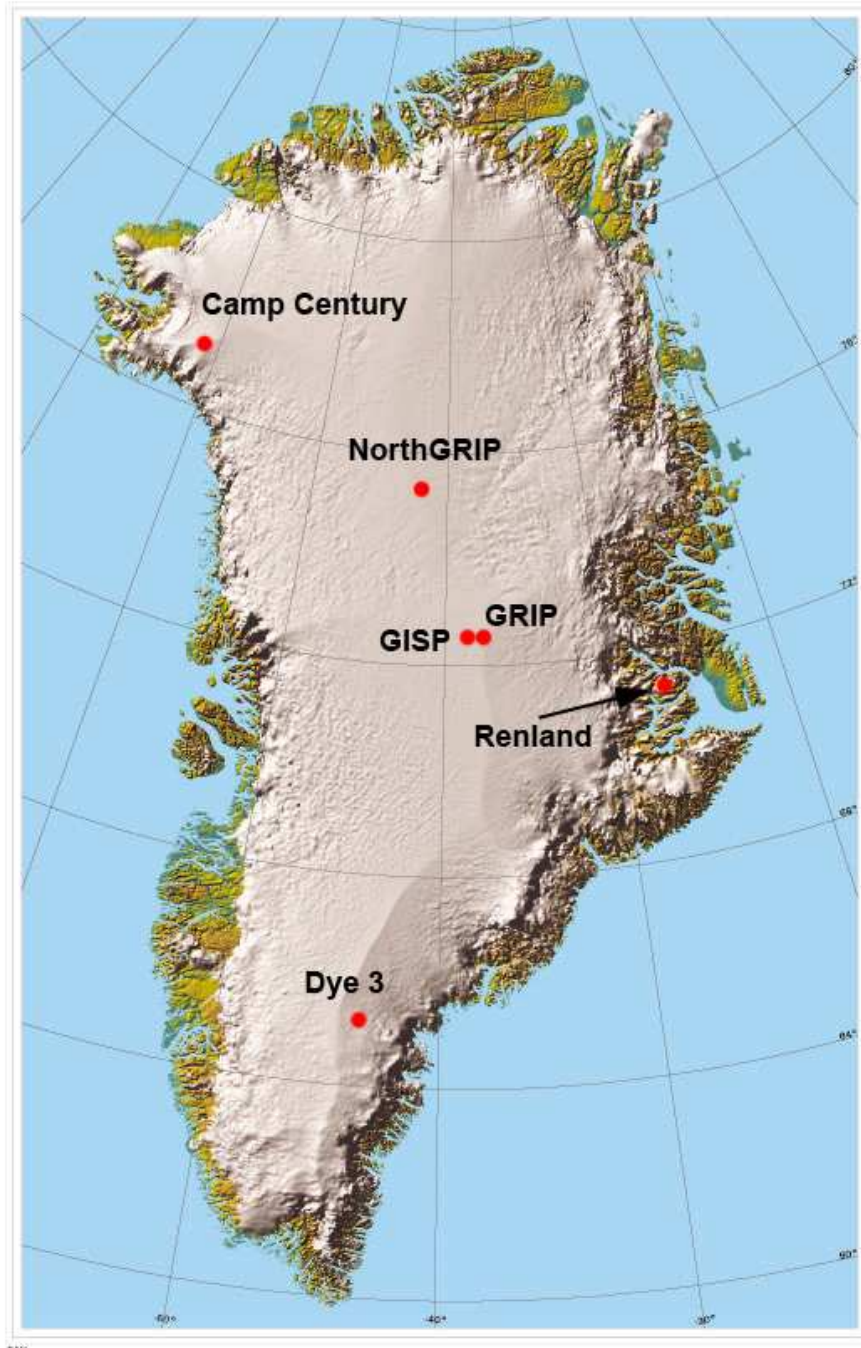


Figure 1.1: The location of six important ice core drill sites in Greenland.  
Map: S. Ekholm, Danish National Survey and Cadastre.

bedrock [Johnsen et al., 1997]. This means that even though the Central Greenland ice cores contain ice from the previous interglacial period – the Eemian (115,000–130,000 years ago) – the chronology of the layers has been broken. Because an undisturbed climate record containing the Eemian and the onset of the glacial period may contribute significantly to the understanding of the behaviour of the present and future climate, it was decided to drill a new core at a location where the conditions were optimal for finding old undisturbed ice. This site was selected according to three criteria:

- It should be located on an ice ridge to ensure minimal horizontal velocity and thereby minimal need to correct for upstream effects.
- The bedrock should be flat in order to minimize flow induced disturbances.
- The accumulation rate should be low in order to find the Eemian layer as high above bedrock as possible, but not so low that the pressure melting temperature is reached at the bottom.

In 1996 drilling was initiated at the NorthGRIP drill site located 75.10°N and 42.32°W, 316 km NNW of GRIP. The ice in the area flows along a NNW-trending ice ridge from GRIP towards NorthGRIP. The surface velocity at NorthGRIP is 1.3 m/yr [Hvidberg et al., 2002], the ice thickness is 3085 m, and the present mean annual temperature and accumulation rate are -31.5°C and 0.193 m/yr, respectively. Before the drilling was initiated models predicted the Eemian layer to be located at depths of 2750–2850 m [Dahl-Jensen et al., 1997]. However, by the end of the 2001 season a depth of 3001 m was reached, and there was no sign of the Eemian. Furthermore, the basal layers did not thin as expected. It was now clear that an unexpectedly high geothermal heat flux raised the temperature to the pressure melting point at the bottom. Basal melting had eaten away the oldest layers and prevented the layers from thinning towards zero at bedrock, as they would have if there had been no melting. In 2003 Eemian ice was encountered immediately above bedrock, but a complete Eemian record was not obtained. However, the unexpectedly high layer thickness in the bottom part of the core offers a unique opportunity to study the transition from the Eemian to the glacial period in very high resolution.

The information contained in the NorthGRIP ice core may contribute significantly to our understanding of the climate system. In order to interpret the climatic information in an ice core it is crucial to establish a depth-age relationship for the core. This is normally not straight forward, since the flow conditions in a given area may have changed significantly during time. In the upper part of an ice core, dating is most precisely done by counting

annual layers, which may be identified from annual variations in the stable isotope composition, in the dust content, and in the concentration of different ions in the ice. This counting process is very laborious, and with depth it gets increasingly difficult to distinguish the layers. Ice flow modelling is therefore the preferred tool for dating old ice from the ice cores. Johnsen et al. [2001] derived the ss09sea timescale for the GRIP ice core by using a one-dimensional flow model constrained by two tie points. This timescale has been transferred to the NorthGRIP ice core by cross-dating the climate records. Thus the existing timescale for the NorthGRIP ice core relies completely on the GRIP dating.

The aim of this thesis is to develop a new timescale for the NorthGRIP ice core, that is less dependent on the ss09sea dating. The approach will be to simulate the flow in the NorthGRIP area with a simple flow model. Several of the flow model parameters – for instance the melt rate – are unknown. Estimates for these parameters can be obtained through an inversion of the flow model, but a set of observed depth-age horizons is needed in order to constrain the inversion. For this purpose I use layers of equal age revealed by radar images. The layers are dated from their observed depths in the NorthGRIP ice core using the ss09sea chronology. From the estimated model parameters a new depth-age relationship is calculated using the flow model. The structure of the thesis is outlined below.

**Chapter 2** gives background information on the structure of the Greenland Ice Sheet. In the first part of the chapter some basic concepts of glaciology are presented, while the cause and nature of the internal layers observed in radar images of the ice sheet are introduced in the second part.

**Chapter 3** deals with ice flow modelling. The flow model and the input it requires are described.

**Chapter 4** is an introduction to inverse Monte Carlo theory, that will be used to invert the flow model. Relevant probability density concepts and concepts from inverse theory are defined, and the inverse Monte Carlo algorithm is deduced.

**Chapter 5** introduces the radio-echo data used to constrain the inversion of the flow model.

**Chapter 6** gathers the information on the physical system at hand and gives an outline of the algorithm used for this particular Monte Carlo inversion.

**Chapter 7** presents the results of the present work.

**Chapter 8** sums up the main conclusions of this thesis.

**Chapter 9** makes a few suggestions for future work with similar models.

## Chapter 2

# Background

This chapter consists of two parts. The first part introduces a few basic glaciological concepts, while the second part gives an overview of the nature of the internal layers that are revealed in the ice by radio-echo sounding.

### 2.1 A Short Introduction to Glaciology

#### 2.1.1 Densification

Newly fallen snow has a density of 50–70 kg/m<sup>3</sup> [Paterson, 1994]. Each layer of snow that falls on the Greenland ice cap is buried by the following snow falls, and as it sinks down into the glacier it is gradually compressed to ice by the weight of the overlying layers. At first the density changes are primarily caused by rounding and settling of the individual grains, but later the most dominant processes are recrystallisation and deformation. At a density of 830 kg/m<sup>3</sup> the interconnecting air passages are closed off and air is now only present in closed bubbles. A further increase in density to 917 kg/m<sup>3</sup> happens when the air in the bubbles is compressed. The stage between snow and ice is called firn, and the transition from firn to ice happens when the air passages are closed off. The rate of transformation from snow to ice depends on temperature and accumulation rate and is thus site specific. In Central Greenland the transition from firn to ice is typically found at a depth of about 70 m [Paterson, 1994]. A plot of the measured density versus depth at NorthGRIP is shown on the left in Fig. 2.1.

In ice flow models the ice equivalent thickness is often used. This is the thickness a layer would attain if it were compressed to ice. By using ice

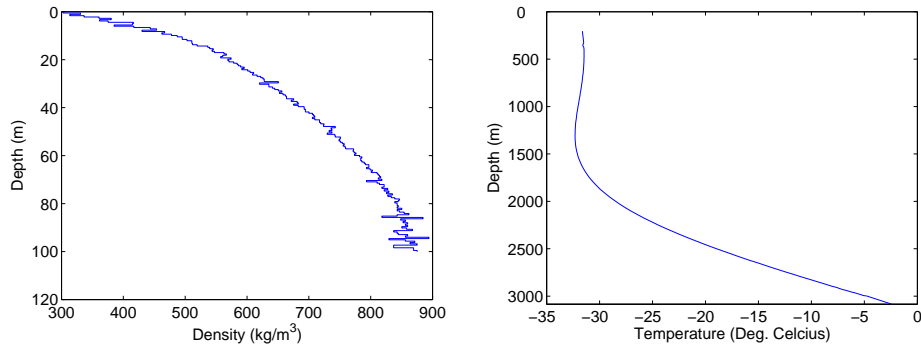


Figure 2.1: **Left:** The density profile for the upper 100 m at NorthGRIP. The pore close off density of  $830 \text{ kg/m}^3$  is seen to be reached at a depth of about 80 m. At 100 m depth the density of glacier ice,  $917 \text{ kg/m}^3$  has not yet been reached. **Right:** The temperature profile from the NorthGRIP borehole. The temperature at the base is at the pressure melting point,  $-2.4^\circ\text{C}$ . The coldest temperatures are found in the middle of the ice sheet, where the cold ice from the Last Glacial Maximum (LGM) is located.

equivalent thicknesses, the densification in the firn layer is ignored. This can only be done if accurate results are not needed for the top part of the ice. In this thesis the focus is on the deep ice, so ice equivalent thicknesses will be used. The air column in the firn in the NorthGRIP area has been estimated to 25 m [D. Dahl-Jensen, pers. comm.]. Thus the ice equivalent ice thickness at NorthGRIP is 25 m lower than the observed thickness of 3085 m, namely 3060 m.

### 2.1.2 Temperatures

Temperature profiles from the Greenland Ice Sheet are known from borehole measurements. After the drilling is finished, the liquid filled hole is left to equilibrate for a couple of seasons. The temperature is then measured with very high accuracy by lowering a logging instrument down into the borehole. The warmest temperatures of the ice sheet are found at the base, because geothermal heat from the bedrock raises the temperature here. Within the glacier, heat is produced by ice deformation, and heat transport is dominated by the downward advection of cold ice from the surface. The surface temperature is determined by the climate, and because ice is a poor heat conductor, remnants of the mean annual surface temperature is preserved in the ice as it sinks down through the ice sheet. Thus past surface temperatures can be found by inversion of the measured borehole temperature profiles [Dahl-Jensen et al., 1998]. The right side of Fig. 2.1 shows the measured temperature profile at NorthGRIP. It is seen that the temperature reaches the pressure melting point of  $-2.4^\circ\text{C}$  at the bottom.

### 2.1.3 $\delta^{18}\text{O}$

More than 99 % of the molecules in natural water are  $\text{H}_2^{16}\text{O}$ , but small amounts of isotopically heavier components like  $\text{H}_2^{18}\text{O}$  are also found. The content of  $\text{H}_2^{18}\text{O}$  in a water (or ice) sample is given by the  $\delta$ -value of the sample:

$$\delta^{18}\text{O} = \frac{R_{\text{sample}} - R_{\text{SMOW}}}{R_{\text{SMOW}}}, \quad R = \frac{[^{18}\text{O}]}{[^{16}\text{O}]}, \quad (2.1)$$

where SMOW is a Standard Mean Ocean Water. Small differences between the vapour pressure of the components causes the  $\text{H}_2^{18}\text{O}$ -molecule evaporate with slightly more difficulty and condense with slightly more ease than the  $\text{H}_2^{16}\text{O}$ -molecule. This leads to a fractionation for evaporation and precipitation processes [Dansgaard, 1964]. Thus as an air mass cools and precipitation is formed, the the remaining vapour will get increasingly more depleted in  $\text{H}_2^{18}\text{O}$  as precipitation forms. The amount of precipitation formed since the last uptake of water depends on the temperature gradient between the source region and the place of deposition. Because temperatures are much more stable over the ocean than over the ice, the content of  $\text{H}_2^{18}\text{O}$  in the ice is strongly dependent on the temperature over the ice. It follows that measuring the  $\delta^{18}\text{O}$ -value along the core gives information on past temperatures over the ice. The  $\delta^{18}\text{O}$  curve for the NorthGRIP ice core is shown in Fig. 3.5.

### 2.1.4 Ice Crystal Structure

The  $\text{H}_2\text{O}$  molecule is shaped like a regular tetrahedron with the oxygen atom in the middle (see Fig. 2.2). The molecule has 10 electrons – eight from the oxygen atom and one from each of the hydrogen atoms. Two electrons from the oxygen atom are located close to the oxygen nucleus in the s-shell. The remaining eight electrons are kept in eccentric orbits, which radiate tetrahedrally from the oxygen nucleus. Two of these orbits contain a hydrogen nucleus (a proton). The electrons do not screen all the positive charge from these, and since there is an excess negative charge in the two orbits with no protons, the ice molecule has two corners with positive charge and two with negative charge. The molecules arrange themselves in layers of hexagonal rings held together by hydrogen bonds between to corners of opposite charges. Thus each molecule is surrounded by four others. The plane of such a layer is called the basal plane of the crystal and the normal to the basal plane is called the c-axis or the optical axis of the crystal.

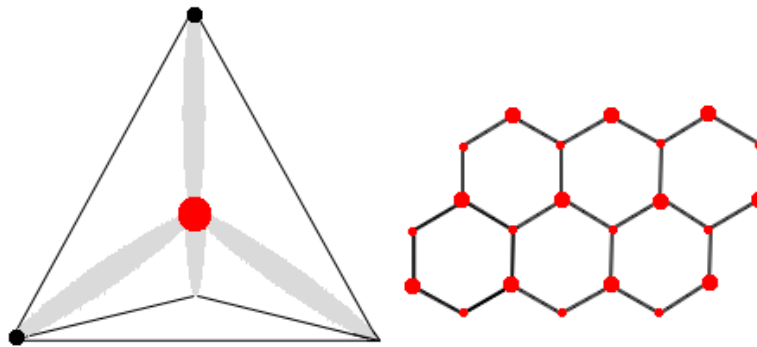


Figure 2.2: **Left:** The  $\text{H}_2\text{O}$  molecule. The oxygen and hydrogen atoms are indicated by red and black dots, respectively. The four eccentric electron orbits are shown as grey ellipses. The angle between two electron orbits is  $104.5^\circ$ . **Right:** The hexagonal structure of an ice crystal. The red dots indicate the positions of the oxygen atoms. The  $104.5^\circ$  angle between the electron orbitals make it impossible for the 6 oxygen atoms in a hexagonal ring to be in the exact same plane. This is indicated by the different sizes of the dots in the figure. The plane of the smaller dots is shifted  $0.0923 \text{ nm}$  from that of the larger dots. This displacement is small compared to the spacing of  $0.276 \text{ nm}$  between basal layers [Paterson, 1994].

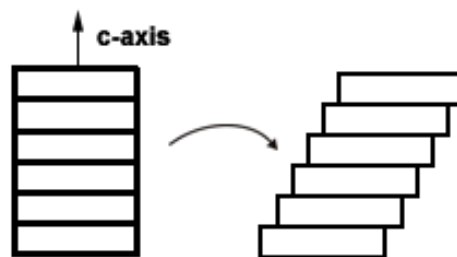


Figure 2.3: If there is a stress component parallel to the basal planes of the crystal, it will deform by gliding on the basal planes.

### 2.1.5 Deformation of Ice

Ice is a quasi-viscous material and it deforms under applied stress. Laboratory studies have revealed that a single ice crystal deforms by gliding on its basal planes (see Fig. 2.3). The gliding is facilitated by the movement of small linear defects in the crystal structure (dislocations). If the crystal is oriented unfavourably for basal gliding – i.e. if there is no stress component parallel to the basal plane – it can still deform, but the stress needed is 100 times higher than that required for basal gliding [Paterson, 1994].

Polycrystalline ice is called isotropic if the  $c$ -axes of the crystals are randomly oriented. In isotropic ice, some crystals are oriented favourably for basal gliding and others are not. This means that polycrystals deform much more slowly than single crystals. The deformation of polycrystalline ice is a

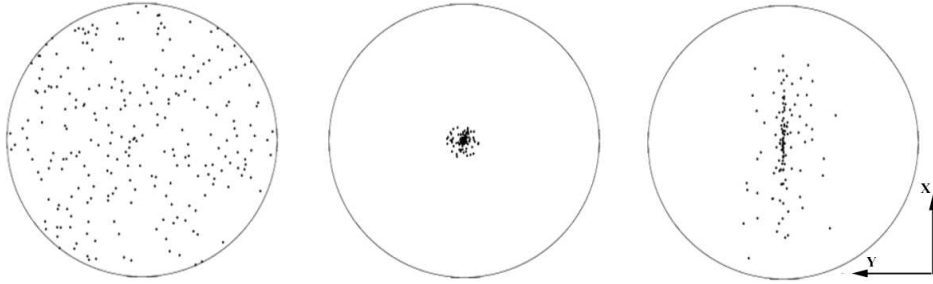


Figure 2.4: Schmidt diagrams for isotropic ice (left), the fabric resulting from simple shear (middle), and the fabric resulting from uniaxial compression confined in the  $x$ -direction (right). The  $x$ - and  $y$ -axes are indicated in the figure. The  $z$ -axis is pointing out of the paper (it is a right-handed coordinate system).

balance between several processes: Dislocation glide, rotation of crystals to make them more optimal for dislocation glide, crystal growth, and dynamic recrystallization. The result of this is that the crystal orientation fabric of the ice changes with depth. In the top of the ice sheet the crystal orientation is random, but as the ice sinks down it is deformed and the rotation of the crystals leads to the formation of an anisotropic fabric. The type of fabric formed depends on the stress conditions at the site. Generally the  $c$ -axes of the crystals rotate towards an axis of compression and away from an axis of extension. Simple shear which is often encountered near the bed in ice sheets, leads to a fabric where the  $c$ -axes are close to the vertical. This is called a strong single maximum fabric. At NorthGRIP the principal surface strain rates have been determined from strain net measurements (see Fig. 3.1) to  $\dot{\epsilon}_1 = (-0.4 \pm 0.6) \cdot 10^{-5} \text{ yr}^{-1}$  and  $\dot{\epsilon}_2 = (7.1 \pm 0.6) \cdot 10^{-5} \text{ yr}^{-1}$  along and transverse to the ridge, respectively [Hvidberg et al., 2002]. The vertical compression is almost balanced by horizontal stretching transverse to the ridge. Thus the stress regime in the upper part of the ice sheet in the NorthGRIP area resembles confined uniaxial compression. This stress configuration leads to a fabric with a single maximum, which is elongated in the confined direction.

The crystal fabric of a polycrystalline aggregate of ice can be represented by a Schmidt diagram. A Schmidt diagram is the equal-area projection onto the plane of the points of intersection between a sphere and the  $c$ -axes when these pass through the centre of the sphere. Schmidt diagrams for isotropic ice and for the fabrics produced by simple shear and confined compression, respectively, are shown in Fig. 2.4.

### 2.1.6 Ice Flow

The deformation of polycrystalline isotropic ice is often described by an empirical relation known as Glen’s flow law [Glen, 1955]

$$\dot{\epsilon}_{ij} = A\tau_e^{n-1}\tau_{ij}, \quad (i, j = x, y, z). \quad (2.2)$$

$\dot{\epsilon}_{ij}$  is the strain rate tensor,  $\tau_e$  is the effective shear stress,  $\tau_{ij}$  is the deviatoric stress tensor,  $n$  is a constant, and  $A$  depends on the in situ conditions. The value of  $n$  is not well known, but the most widely used value for ice modelling is  $n = 3$  [Paterson, 1994]. The variation of  $A$  with temperature  $T$  follows the Arrhenius relation

$$A = A_0 \exp\left(\frac{-E}{RT}\right), \quad (2.3)$$

where  $A_0$  is independent of temperature,  $R = 8.314 \text{ J}/(\text{mol}\cdot\text{K})$  is the gas constant, and  $E$  is the activation energy for deformation.

The development of an anisotropic fabric with depth significantly affects the ice flow. In the case of a strong single maximum fabric which is often encountered in the ice sheet, the ice gets “harder” for vertical compression and “softer” for simple shear because most crystals are oriented with their basal planes close to the horizontal. Glen’s law is ill suited to describe the flow of anisotropic ice. Several flow laws for anisotropic materials have been published e.g. Johnson [1977] and Azuma [1994]. These models are complicated compared to Glen’s law.

Ice flow laws like the ones mentioned above are used in general models of the ice sheet. In this thesis a different approach is adopted, because we have detailed knowledge about the accumulation rate, the bedrock- and surface topography, and the horizontal surface velocity in the area of interest. This makes it possible to use a model specially tuned to these conditions. A model called the Dansgaard-Johnsen model has proven to be very useful. In this study a modified version of the Dansgaard-Johnsen model is used. This model is presented in Chapter 3.

## 2.2 Internal Layers in Ice

Since the early 1960s airborne radio-echo sounding (RES) has been used to obtain information on ice thicknesses of smaller glaciers as well as the Greenland and Antarctic ice sheets, see Gogineni et al. [1998] for a historical overview. In addition to the ice surface and the bedrock, a number of internal layers in the ice are often seen in the recovered radar images (see Fig. 5.2). In Greenland these layers can be traced continuously for hundreds of kilometers [Gudmandsen, 1975, Chuah et al., 1996].

### 2.2.1 The Basic Equations

The internal layers appear on the images because they reflect a larger part of the radar waves than the surrounding ice. For an ice layer of thickness  $l$  and admittance  $Y + \Delta Y$  embedded in ice of admittance  $Y$ , the power reflection coefficient  $R$  is given by Paren and Robin [1975] as

$$R = 4 \sin^2 \left( \frac{2\pi l}{\lambda_m} \right) \cdot \left| \frac{1}{2} \frac{\Delta Y}{Y} \right|^2, \quad (2.4)$$

where  $\lambda_m$  is the wavelength of the radar in ice. Since

$$Y = i\omega C_0 \epsilon, \quad (2.5)$$

where  $i$  denotes the imaginary unit,  $\omega$  is the angular frequency,  $C_0$  is the geometrical capacitance, and  $\epsilon$  is the complex permittivity of the ice. Eq. (2.4) may be rewritten as

$$R = 4 \sin^2 \left( \frac{2\pi l}{\lambda_m} \right) \cdot \left| \frac{1}{2} \frac{\Delta \epsilon}{\epsilon} \right|^2. \quad (2.6)$$

It is seen from Eq. (2.6) that layers of different power reflection coefficients must have different complex permittivities. Thus the studies of the complex permittivity of the ice may provide valuable information on the nature of the observed layers. The complex permittivity is given by

$$\epsilon = \epsilon' + i\epsilon'', \quad (2.7)$$

where  $\epsilon'$  is the dielectric constant and  $\epsilon''$  is the relative loss factor. This may also be written as

$$\epsilon = \epsilon'(1 - i \tan \delta), \quad (2.8)$$

where

$$\tan \delta = \frac{\epsilon''}{\epsilon'} = \frac{\sigma}{\omega \epsilon_0 \epsilon'}. \quad (2.9)$$

$\delta$  is the phase angle between the displacement current and the total current in an alternating electric field,  $\sigma$  is the dielectrical conductivity (not to be confused with the direct current conductivity  $\sigma_{d.c.}$ , though this contributes to  $\sigma$ ), and  $\epsilon_0$  is the permittivity of free space.  $\tan \delta$  is known as the “loss tangent” because it describes the absorption of electromagnetic energy in the ice. From Eq. (2.8) it is seen that  $\epsilon$  will be affected by changes in either the dielectric constant  $\epsilon'$  or in the loss tangent [Evans, 1965, Bogorodsky et al., 1985].

### 2.2.2 The Cause of Increased Reflection

There has been some dispute as to the cause of the changes in  $\epsilon$ . Several authors conclude that the most likely cause of the shallow reflectors is changes in  $\epsilon'$  due to density changes [Harrison, 1973, Paren and Robin, 1975, Clough, 1977], but Hammer [1980] and Hempel et al. [2000] find that changes in loss tangent caused by raised impurity levels from volcanic fall out is the best explanation. As to the deep reflectors there seems to be a general agreement that density changes alone can not explain the strength of the observed reflections [Harrison, 1973, Paren and Robin, 1975]. Paren and Robin [1975] find that changes in loss tangent is the most likely explanation for the deep reflectors. This is supported by the works of Hammer [1980], Millar [1981], and Hempel et al. [2000], who find that reflectors and layers of increased acidity from major volcanic events are found at the same depths, and that the resulting changes in loss tangent are sufficient to explain the observed power reflection coefficients. However, Harrison [1973] and Fujita and Mae [1994] argue that the primary cause of the deep reflectors is changes in  $\epsilon'$  due to changes in crystal orientation. Fujita et al. [1999] used the fact that the loss tangent – but not the dielectric constant – is frequency dependent to estimate the relative importance of changes in these two parameters. Through a two-frequency radar experiment carried out in East Antarctica they found that changes in the loss tangent dominate at intermediate depths while changes in fabric dominate at greater depths.

Fig. 2.5 shows the NorthGRIP ECM (electrical conductivity measurement) curve, the radio-echo image and the NorthGRIP  $\delta^{18}\text{O}$  curve on the same depth scale. The reflecting layers are seen to coincide with major changes in the ECM level, which again coincide with abrupt changes in the climate curve (the  $\delta^{18}\text{O}$  curve). The ECM curve is a measure of the direct conductivity of the ice. Thus NorthGRIP data indicate that the deep reflectors are caused by varying impurity content in connection with abrupt climate changes.

### 2.2.3 Interpretation of the Layers

Even though there is disagreement on the cause of the permittivity changes of the internal reflectors, there is a general consensus that they represent former deposition surfaces [Gudmandsen, 1975, Bogorodsky et al., 1985]. This means that they are layers of equal age – *isochrones*. Thus the radar images may provide valuable information on the ice flow pattern throughout the ice sheet. Indeed, if layers have been dated from their observed depths in an ice core, knowledge on the depth-age relationship can be invoked at locations far from the drill site by following the internal layers. This information may

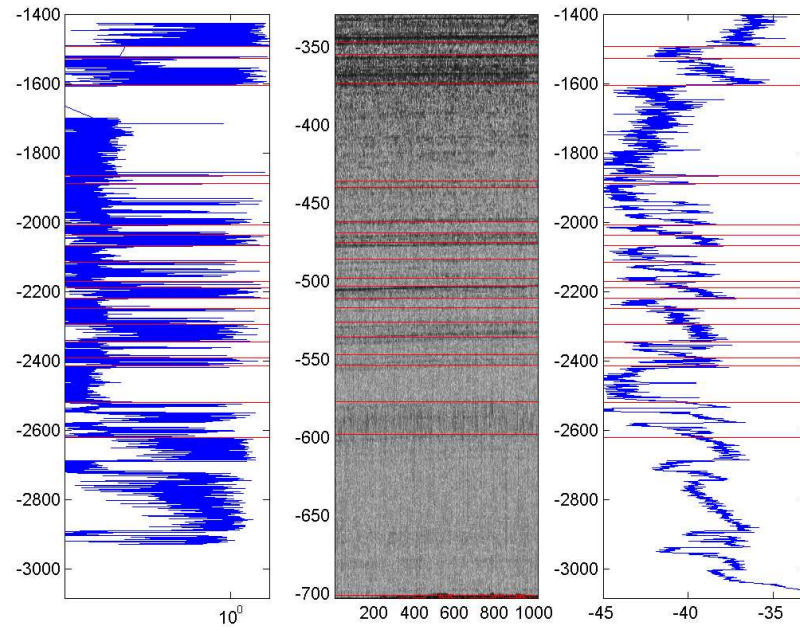


Figure 2.5: **Left:** The ECM curve for the lower part of the NorthGRIP ice core. **Middle:** The radio-echo image. **Right:** The lower part of the  $\delta^{18}\text{O}$  curve from NorthGRIP. The red lines indicate isochrones observed in the radio-echo image. These are seen to coincide with major changes in the ECM level connected to abrupt climate changes. Figure from D. Dahl-Jensen [pers. comm.]

help in deciding new locations for deep ice core drilling as was the case with the NorthGRIP drill site [Dahl-Jensen et al., 1997]. In the present study the layers will be used to constrain a Monte Carlo inversion of the flow model used to simulate the flow in the vicinity of NorthGRIP.

## Chapter 3

# Modelling the Ice Flow

### 3.1 The Flow in the NorthGRIP Area

In the period 1996–2001 a strain net was established around the NorthGRIP drill site (see Fig. 3.1). The surface velocity was determined to  $1.329 \pm 0.015$  m/yr along the ridge, and the principal surface strain rates to  $\dot{\epsilon}_1 = (-0.4 \pm 0.6) \cdot 10^{-5} \text{ yr}^{-1}$  and  $\dot{\epsilon}_2 = (7.1 \pm 0.6) \cdot 10^{-5} \text{ yr}^{-1}$  along and transverse to the ridge, respectively (cf. Section 2.1.5) [Hvidberg et al., 2002]. The horizontal velocity is almost constant along the ridge.

As a result of the horizontal velocity, the ice found in the NorthGRIP ice core was not deposited at the site. It fell as snow upstream from NorthGRIP and was then transported along the ridge. The deeper a layer is found in the core, the longer is the horizontal distance it has travelled. Dahl-Jensen et al. [2003] estimated that the ice found at a depth of 2850 in the NorthGRIP ice core was deposited 50 km upstream from the drill site. The melt rate is believed to vary along the flow line (cf. Chapter 5). This implies that the ice found in the NorthGRIP ice core has experienced different melt rates during the past. Thus a one-dimensional flow model will not suffice when a dating of the ice core is wanted. A two-dimensional model is required in order to incorporate the varying melt rates along the line.

### 3.2 The Flow Model

In the present study a simple two-dimensional model is used to simulate the flow along the ice ridge in the vicinity of NorthGRIP. For this purpose a coordinate system with the  $x$ -axis along the ridge pointing in the direction

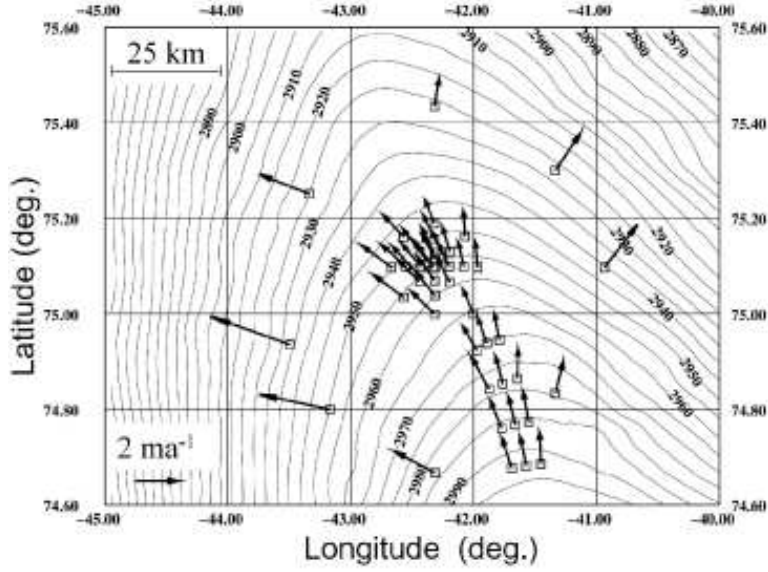


Figure 3.1: Observed surface velocities around the NorthGRIP drill site ( $75.10^{\circ}\text{N}$ ,  $42.32^{\circ}\text{W}$ ). Figure from Hvidberg et al. [2002].

of the flow, and the  $z$ -axis pointing upwards is adopted. The origin of this coordinate system is placed at GRIP at sealevel. This study has been limited to concern a 100 km section of the ridge starting 80 km upstream from NorthGRIP and ending 20 km downstream.

The model that will be used to simulate the flow along the ridge is a Dansgaard-Johnsen type model [Dansgaard and Johnsen, 1969]. This model was originally developed to model the time scale for the Camp Century drill site in Northern Greenland (see Fig. 1.1). It is widely used because it provides good results and has few model parameters. At Camp Century the ice is frozen to the bed, so the original model does not account for basal melting and sliding. In order to use the model for the flow in the NorthGRIP area where melting is known to occur, it has been modified to account for these two things.

The Dansgaard-Johnsen model is based on the assumption that the horizontal velocity is constant from the surface down to a height  $h$  above bedrock. From here it decreases linearly to the sliding velocity at the bottom (see Fig. 3.2)

$$u(x, z) = \begin{cases} u_{\text{sur}}(x) & z \in [h, H] \\ u_{\text{sur}}(x) (F_B + (1 - F_B) \frac{z}{h}) & z \in [0, h[ \end{cases}, \quad (3.1)$$

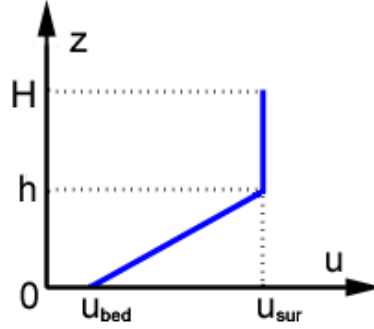


Figure 3.2: The horizontal velocity profile assumed in the Dansgaard-Johnsen model.

where  $u$  is the horizontal velocity,  $u_{\text{sur}}$  is the horizontal surface velocity,  $H$  is the ice thickness in ice equivalent,  $z$  is the ice equivalent height above bedrock, and  $F_B = \frac{u_{\text{bed}}}{u_{\text{sur}}}$  is the fraction of basal sliding.  $h$  is called the kink height.

If the ice is assumed to be incompressible we can use the continuity equation

$$\frac{\partial u}{\partial x} + \frac{\partial w}{\partial z} = 0 \quad \Leftrightarrow \quad \frac{\partial w}{\partial z} = -\frac{\partial u}{\partial x}, \quad (3.2)$$

where  $w$  is the vertical velocity. Differentiation of Eq. (3.1) gives

$$\frac{\partial w}{\partial z} = -\frac{\partial u}{\partial x} = \begin{cases} -\frac{\partial u_{\text{sur}}}{\partial x} & z \in [h, H] \\ -\frac{\partial u_{\text{sur}}}{\partial x} (F_B + (1 - F_B) \frac{z}{h}) & z \in [0, h[ \end{cases}. \quad (3.3)$$

The vertical velocity can now be calculated by integration of Eq. (3.3)

$$w(z) = \begin{cases} w_b - \frac{\partial u_{\text{sur}}}{\partial x} (z - \frac{1}{2}h(1 - F_B)) & z \in [h, H] \\ w_b - \frac{\partial u_{\text{sur}}}{\partial x} (F_B z + \frac{1}{2}(1 - F_B) \frac{z^2}{h}) & z \in [0, h[ \end{cases}, \quad (3.4)$$

where  $w_b$  is the basal melt rate (the vertical velocity at the base). Volume conservation on an ice column (See Fig. 3.3) gives:

$$\frac{\partial H}{\partial t} = a + w_b - \frac{\partial(H \cdot u_{\text{mean}})}{\partial x}, \quad (3.5)$$

where  $t$  is time,  $a$  is annual ice equivalent accumulation, and  $u_{\text{mean}}$  is the mean horizontal velocity over the entire height of the ice column.  $u_{\text{mean}}$  is found by integration of Eq. (3.1), such that

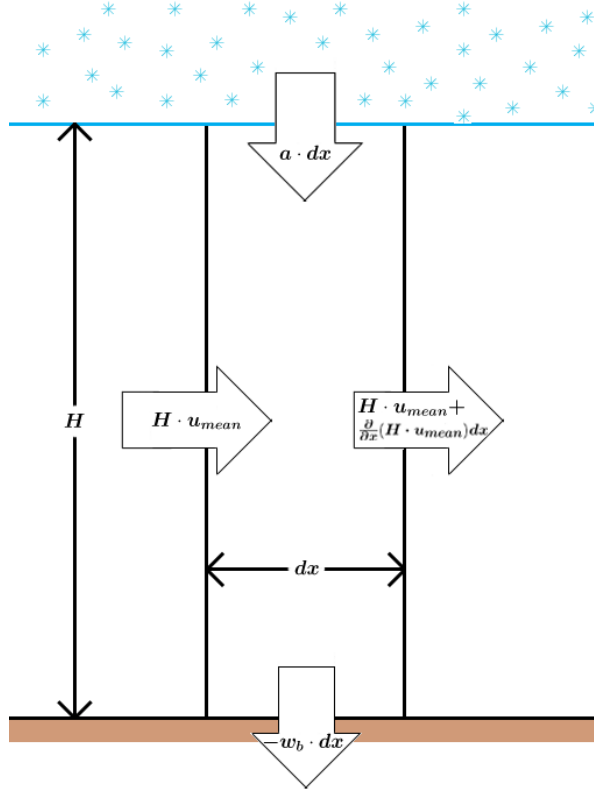


Figure 3.3: Conservation of volume on an ice column.

$$u_{\text{mean}} = \frac{1}{H} \int_0^H u(z) dz \quad \Rightarrow \quad H \cdot u_{\text{mean}} = u_{\text{sur}} \left( H - \frac{1}{2} h (1 - F_B) \right). \quad (3.6)$$

Inserting Eq. (3.6) into Eq. (3.5) gives

$$\frac{\partial H}{\partial t} = a + w_b - \frac{\partial u_{\text{sur}}}{\partial x} \left( H - \frac{1}{2} h (1 - F_B) \right). \quad (3.7)$$

Assuming constant ice thickness during time ( $\frac{\partial H}{\partial t} = 0$ ), the following expression for  $\frac{\partial u_{\text{sur}}}{\partial x}$  is found from Eq. (3.7)

$$\frac{\partial u_{\text{sur}}}{\partial x} = \frac{a + w_b}{H - \frac{1}{2} h (1 - F_B)}. \quad (3.8)$$

From Eqs. (3.1), (3.4), and (3.8) it is seen that in order to calculate the velocity at a given point in the ice cap, the following parameters must be

known: The horizontal surface velocity  $u_{\text{sur}}$ , the kink height  $h$ , the fraction of basal sliding  $F_B$ , the ice thickness  $H$ , the basal melt rate  $w_b$ , and the accumulation rate  $a$ . In the following, all parameters except the latter are assumed to be independent of time. Furthermore the basal melt rate is assumed to be constant over intervals of 8 km, and the kink height and the fraction of bottom sliding are assumed linearly dependent on the basal melt rate:

$$h = \alpha \cdot w_b + h_0 \quad (3.9)$$

and

$$F_B = \beta \cdot w_b + F_{B0}. \quad (3.10)$$

When the ice is frozen to the bed ( $w_b = 0$ ) there will be no basal sliding. Thus  $F_{B0} = 0$  and Eq. (3.10) is reduced to

$$F_B = \beta \cdot w_b. \quad (3.11)$$

The parameters  $\alpha$ ,  $h_0$ , and  $\beta$  are unknown and will be determined through a Monte Carlo inversion of the flow model.  $H$  is known from radio-echo sounding measurements [Chuah et al., 1996, Gogineni et al., 1998, Gogineni et al., 2001, Kanagaratnam et al., 2001], and  $u_{\text{sur}}(x)$  is known from the NorthGRIP strain net measurements [Hvidberg et al., 2002]. Estimates of the present accumulation rates along the line  $a(t_{\text{present}}, x)$  have been made from shallow core studies [Dahl-Jensen et al., 1997]. Fig. 3.4 shows a plot of  $H$ ,  $u_{\text{sur}}$ , and  $a$ . In the following it will be assumed that the ratio between the accumulation at NorthGRIP and that at other locations along the flow line has remained unchanged during time, that is

$$a(t, x) = a(t, x_{\text{NGRIP}}) \cdot \frac{a(t_{\text{present}}, x)}{a(t_{\text{present}}, x_{\text{NGRIP}})}. \quad (3.12)$$

$a(t, x_{\text{NGRIP}})$  is calculated from the accumulation model presented in the following section.

### 3.3 The Accumulation Model

The modified Dansgaard-Johnsen model presented above requires the accumulation rate history as input. The past accumulation rates are calculated

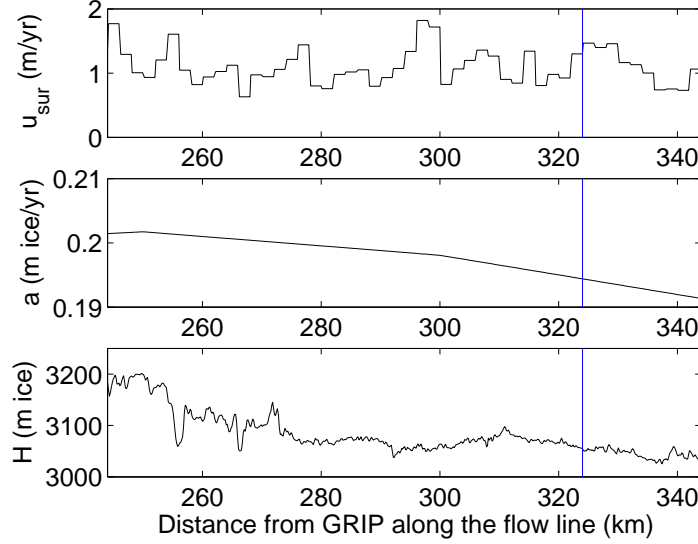


Figure 3.4: From the top: The surface velocity, the present annual accumulation rate, and the ice thickness along the ice ridge. The position of the NorthGRIP drill site is indicated by the blue line.

using a model of the same type as the one used by Johnsen et al. [1995] to date the GRIP ice core: The time dependent ice equivalent accumulation rate  $a(t)$  is calculated from the measured  $\delta^{18}\text{O}$ -values

$$a(t) = a_0 \cdot e^{k_2(\delta^{18}\text{O}(t) - \delta^{18}\text{O}_w) + \frac{1}{2}k_1(\delta^{18}\text{O}(t)^2 - \delta^{18}\text{O}_w^2)} \quad (3.13)$$

$$k_1 = \frac{c_1 - c_2}{\delta^{18}\text{O}_w - \delta^{18}\text{O}_c}, \quad k_2 = c_1 - \delta^{18}\text{O}_w \cdot k_1, \quad (3.14)$$

where  $a_0 = 0.193$  m/yr is the present ice equivalent accumulation rate at NorthGRIP, and  $\delta^{18}\text{O}_w = -35.2\text{‰}$  and  $\delta^{18}\text{O}_c = -42\text{‰}$  are typical  $\delta^{18}\text{O}$  values for warm and cold climate at NorthGRIP, respectively.  $c_1$  and  $c_2$  denote the relative slopes of  $a$  in warm and cold climate, respectively:

$$c_1 = \left. \frac{1}{a} \frac{\partial a}{\partial \delta^{18}\text{O}} \right|_{\delta^{18}\text{O}_w}, \quad c_2 = \left. \frac{1}{a} \frac{\partial a}{\partial \delta^{18}\text{O}} \right|_{\delta^{18}\text{O}_c}. \quad (3.15)$$

The parameters  $c_1$  and  $c_2$  are unknown and will be determined by the Monte Carlo inversion.

The  $^{18}\text{O}$  content of the ice from the ice core has been measured relative to the SMOW standard (Standard Mean Ocean Water). During the glacial period massive amounts of water were stored as ice on the continents causing a eustatic sealevel lowering of the order of 120 m compared to present

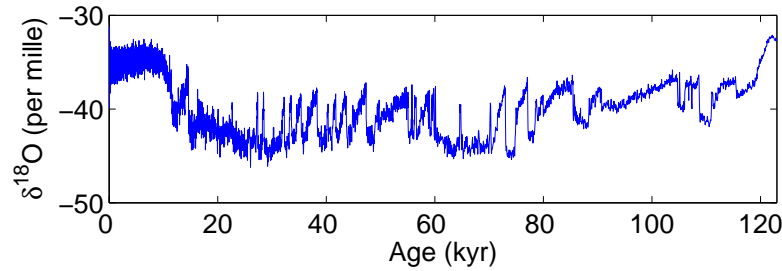


Figure 3.5: The measured NorthGRIP  $\delta^{18}\text{O}$  record plotted on the ss09sea timescale in 50 years resolution. [Johnsen et al., 2001].

conditions [Fairbanks, 1989]. Since the water was removed from the oceans by evaporation, the  $\delta^{18}\text{O}$  value of the ocean water was positive during the glacial period as opposed to 0 at present. Waelbroeck et al. [2002] have derived past changes in sealevel and ocean  $\delta^{18}\text{O}$  from benthic foraminifera. These ocean  $\delta^{18}\text{O}$  values have been used to correct the measured NorthGRIP  $\delta^{18}\text{O}$  curve for the effect of the changes in ocean  $\delta^{18}\text{O}$ .

The timescale used for the  $\delta^{18}\text{O}$  curve is the ss09sea timescale, that was developed for the GRIP ice core and then transferred to the NorthGRIP ice core [Johnsen et al., 2001]. Fig. 3.5 shows the NorthGRIP  $\delta^{18}\text{O}$  curve plotted on this timescale. It is seen that the ss09sea chronology predicts an age of 123 kyr (kiloyears) at the bottom at NorthGRIP. Thus the accumulation history obtained from the model described above reaches 123 kyr back in time

### 3.4 Computational Approach

This model is used to simulate the flow along the line in the following way: A modelled isochrone is started at the surface 123 kyr ago and followed as it sinks down through the ice sheet. For every time step the position of the modelled isochrone is stored.

If all the input parameters to the flow model were known, a timescale for the ice could be derived directly from the model, but as described in this chapter, 18 input parameters are unknown:  $\alpha$ ,  $h_0$ ,  $\beta$ , 13 values for the melt rate, and  $c_1$  and  $c_2$ . These parameters will be determined from a Monte Carlo inversion of the flow model. This inversion technique and its direct application to the problem at hand are described in the next chapters.

A one-dimensional version of the flow model presented above is obtained by disregarding the horizontal velocity component. This one-dimensional

model will also be inverted in order to illustrate the advantages of using a two-dimensional model.

## Chapter 4

# Monte Carlo Inversion Theory

Several model parameters for the model presented in the previous chapter are unknown, and I wish to derive estimates for them by using a Monte Carlo method to invert the flow model. This chapter gives an introduction to inverse Monte Carlo theory. Relevant concepts of inverse theory and probability densities are described and the Monte Carlo algorithm is deduced.

### 4.1 Inverse Problems

Consider a system described by a model with a finite number of model parameters and by data obtained by observing the system. Ignoring the measuring noise, the relationship between data and model parameters can be expressed as

$$\mathbf{d} = \mathbf{g}(\mathbf{m}), \quad (4.1)$$

where  $\mathbf{d} \in \mathbb{R}^m$  and  $\mathbf{m} \in \mathbb{R}^n$  are vectors containing the exact data and the model parameters, respectively, and  $\mathbf{g}$  is a vector operator representing the model. The problem of solving Eq. (4.1) for the data vector  $\mathbf{d}$  is called the forward problem: Given a model with known model parameters the data are predicted. However, in geophysics it is more often the case that the data are known from measurements and the model parameters are unknown. In that case Eq. (4.1) needs to be solved for  $\mathbf{m}$ . This is called the inverse problem: Given a model and observed data the model parameters are calculated. The inverse problem can be expressed as

$$\mathbf{m} = \mathbf{g}^{-1}(\mathbf{d}), \quad (4.2)$$

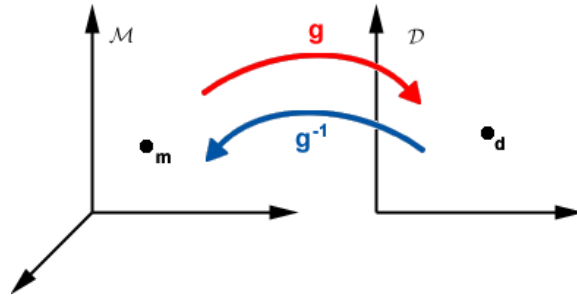


Figure 4.1: The mapping of the model vector  $\mathbf{m}$  from the model space  $\mathcal{M}$  into the data vector  $\mathbf{d}$  in the data space  $\mathcal{D}$  by the operator  $\mathbf{g}$ . The inverse operator  $\mathbf{g}^{-1}$  performs the opposite mapping.

where  $\mathbf{g}^{-1}$  is the inverse of the operator  $\mathbf{g}$  in Eq. (4.1). If the vectors  $\mathbf{d}$  and  $\mathbf{m}$  are considered as points in the data space  $\mathcal{D}$  and the model space  $\mathcal{M}$ , respectively, the operator  $\mathbf{g}$  performs a mapping from  $\mathcal{M}$  into  $\mathcal{D}$ . The dimensions of  $\mathcal{D}$  and  $\mathcal{M}$  need not be the same, and generally they are not. In order to solve the inverse problem in Eq. (4.2) we need to construct the inverse operator  $\mathbf{g}^{-1}$  which performs the mapping from  $\mathcal{D}$  into  $\mathcal{M}$  (see Fig. 4.1). Simple linear inverse problems may be solved using damped least squares or singular value decomposition [Menke, 1989]. However, most geophysical problems are not simple, and it is often impossible to construct the inverse operator  $\mathbf{g}^{-1}$ . Indeed, sometimes even the relation  $\mathbf{g}$  is not given explicitly but exists only in form of a numerical algorithm. In that case the inverse problem must be solved in another way, e.g. by the Monte Carlo method. In order to explain the Monte Carlo method, some concepts from probability theory are introduced below.

## 4.2 Introducing Probability Densities

In the following all expressions for probability density functions will be given without a possible multiplicative constant.

In Section 4.1 we ignored the measurement noise and considered only the exact theory (4.1). Accounting for the noise Eq. (4.1) becomes

$$\mathbf{d}_{\text{obs}} = \mathbf{g}(\mathbf{m}) + \mathbf{n} \quad (4.3)$$

where  $\mathbf{d}_{\text{obs}} \in \mathbb{R}^m$  and  $\mathbf{n} \in \mathbb{R}^m$  are vectors containing the observed data and the noise, respectively. As measurements can never provide us with the exact data vector it is not practical to view  $\mathbf{d}$  and  $\mathbf{m}$  as points in  $\mathcal{D}$  and  $\mathcal{M}$ . A better approach is to work with a probability density function  $\rho(\mathbf{d}, \mathbf{m})$  in the system space  $\mathcal{S}$  given by the Cartesian product of the data

and model spaces. All a priori information – all the information we have before any mathematical analysis – is contained in  $\rho$ , which is called the a priori probability density function. A priori information consists of the observed data, their uncertainties and constraints on the model parameters [Tarantola and Valette, 1982]. The case of no a priori information is represented by the null information function  $\mu$ . The concept of null information is best illustrated through two examples:

1. Assume that we wish to determine the position of the highest point on the Greenland ice sheet from satellite altimeter data. The probability function  $\mu_1$  containing the least information on the location of the highest point must be one that assigns the same probability  $dP$  to any area increment  $dA$  no matter where on the ice sheet it is located:  $dP = \text{constant} \cdot dA$ . Using Cartesian coordinates  $dA = dx dy$ , and the null information function becomes  $\mu_1 = \text{const}$ .
2. Now assume we want to measure the wavelength  $\lambda$  of a ray of electromagnetic radiation. Let  $\mu_\lambda(\lambda)$  be the null information function for the wavelength. The frequency  $\nu$  of the radiation is given by  $\nu = c/\lambda$ , where  $c$  is the speed of light. If  $\mu_\nu(\nu)$  denote the null information function for the frequency we have

$$\mu_\nu(\nu) = \mu_\lambda(\lambda) \left| \frac{d\lambda}{d\nu} \right| = \frac{c}{\nu^2} \mu_\lambda(\lambda). \quad (4.4)$$

As  $\lambda$  and  $\nu$  are equivalent parameters their null information functions must have the same form. From Eq. (4.4) we then have  $\mu_\lambda(\lambda) = \frac{\text{constant}}{\lambda}$  and  $\mu_\nu(\nu) = \frac{\text{constant}}{\nu}$ .

Variables with constant null information functions are called *Cartesian*. Through a simple change of variables from  $\lambda$  and  $\nu$  to  $\log \lambda$  and  $\log \nu$  the variables from Example 2 become Cartesian.

The theoretical relationship  $\mathbf{g}$  between the data and the model parameters is not exact but merely a simplified description of the real world. Even given the model parameters  $\mathbf{m}$ , we are not able to calculate the *true* values for  $\mathbf{d}$ . We therefore replace the exact theory with a theoretical probability density function  $\theta(\mathbf{d}, \mathbf{m})$ . This may be interpreted as “putting error bars on the exact theory” [Tarantola and Mosegaard, 2000].

All our information is now contained in the probability density functions  $\rho$  and  $\theta$ . A new state of information is given by the conjunction of these

$$\sigma(\mathbf{d}, \mathbf{m}) = \frac{\rho(\mathbf{d}, \mathbf{m})\theta(\mathbf{d}, \mathbf{m})}{\mu(\mathbf{d}, \mathbf{m})}. \quad (4.5)$$

$\sigma$  is the a posteriori probability density function. The a posteriori marginal probability density functions are given by

$$\sigma_d(\mathbf{d}) = \int \frac{\rho(\mathbf{d}, \mathbf{m})\theta(\mathbf{d}, \mathbf{m})}{\mu(\mathbf{d}, \mathbf{m})} d\mathbf{m} \quad (4.6)$$

and

$$\sigma_m(\mathbf{m}) = \int \frac{\rho(\mathbf{d}, \mathbf{m})\theta(\mathbf{d}, \mathbf{m})}{\mu(\mathbf{d}, \mathbf{m})} d\mathbf{d}, \quad (4.7)$$

where  $\sigma_d$  and  $\sigma_m$  are the a posteriori probability density functions in  $\mathcal{D}$  and  $\mathcal{M}$ , respectively. Eq. (4.6) solves the general forward problem and Eq. (4.7) solves the general (non-linear) inverse problem [Tarantola and Valette, 1982].

### 4.3 The Likelihood Function

Assume we have a data set  $\mathbf{d}$  and a non-linear model with model parameters  $\mathbf{m}$ , and that the a priori information and theoretical knowledge are contained in  $\rho(\mathbf{d}, \mathbf{m})$  and  $\theta(\mathbf{d}, \mathbf{m})$ , respectively. We seek a posteriori information on the model parameters. Thus we need to solve Eq. (4.7). If the a priori information on  $\mathbf{d}$  and  $\mathbf{m}$  is independent we have

$$\rho(\mathbf{d}, \mathbf{m}) = \rho_d(\mathbf{d})\rho_m(\mathbf{m}) \quad (4.8)$$

and

$$\mu(\mathbf{d}, \mathbf{m}) = \mu_d(\mathbf{d})\mu_m(\mathbf{m}). \quad (4.9)$$

The theory  $\mathbf{g}$  puts no constraints on  $\mathbf{m}$ . Therefore we have

$$\theta(\mathbf{d}, \mathbf{m}) = \theta(\mathbf{d}|\mathbf{m})\mu_m(\mathbf{m}), \quad (4.10)$$

where  $\theta(\mathbf{d}|\mathbf{m})$  is the conditional theoretical probability density function, that is, the theoretical probability density function for  $\mathbf{d}$  given  $\mathbf{m}$ . From Eqs. (4.7), (4.8), (4.9), and (4.10) we get

$$\sigma_m(\mathbf{m}) = \rho_m(\mathbf{m}) \int \frac{\rho_d(\mathbf{d})\theta(\mathbf{d}|\mathbf{m})}{\mu_d(\mathbf{d})} d\mathbf{d}. \quad (4.11)$$

Defining the likelihood function

$$L(\mathbf{m}) \equiv \int \frac{\rho_d(\mathbf{d})\theta(\mathbf{d}|\mathbf{m})}{\mu_d(\mathbf{d})} d\mathbf{d} \quad (4.12)$$

we have

$$\sigma_m(\mathbf{m}) = \rho_m(\mathbf{m})L(\mathbf{m}). \quad (4.13)$$

The likelihood function can be interpreted as a measure of the agreement between the observed data and the data calculated from the model parameters

[Mosegaard, 1998]. Assuming Gaussian uncertainties the likelihood function takes the form

$$L(\mathbf{m}) = e^{-S(\mathbf{m})}, \quad (4.14)$$

where  $S(\mathbf{m})$  is the misfit function given by

$$S(\mathbf{m}) = \frac{1}{2} \sum_i \frac{(d_i - g_i(\mathbf{m}))^2}{s_i^2} \quad (4.15)$$

Here  $s_i$  denotes the uncertainty on a data point  $d_i$ .

## 4.4 The Inverse Monte Carlo Algorithm

The general inverse problem is now reduced to determining  $\rho_m(\mathbf{m})$  and  $L(\mathbf{m})$  over the entire model space, but as this is usually of high dimension it may be a considerable task. Moreover, evaluation of  $\mathbf{g}(\mathbf{m})$  may only be possible through a time consuming numerical algorithm. However, the necessary amount of work can be considerably reduced if a Monte Carlo method is used. A Monte Carlo method is an algorithm that uses random numbers to solve a computational problem. More precisely, we will construct a random walk that samples the model space according to the a posteriori distribution  $\sigma_m$  (importance sampling). A random walk is characterized by the conditional transition probability  $P(\mathbf{m}_i|\mathbf{m}_j)$  that the next step will take us to  $\mathbf{m}_i$  if we are currently at  $\mathbf{m}_j$ . The unconditional probability  $P(\mathbf{m}_i, \mathbf{m}_j)$  that the next step will be from  $\mathbf{m}_j$  to  $\mathbf{m}_i$  is given by

$$P(\mathbf{m}_i, \mathbf{m}_j) = P(\mathbf{m}_i|\mathbf{m}_j)p(\mathbf{m}_j), \quad (4.16)$$

where  $p$  is the equilibrium probability of the random walk [Mosegaard and Tarantola, 1995]. The equilibrium probability is unique if it is possible for the random walk to go from any one point in the model space to any other in a sufficient amount of steps [Feller, 1970].

Our goal is to construct a random walk with equilibrium probability density  $\sigma_m$ . Assume that after a number of steps the equilibrium has been reached. We want to maintain this equilibrium if we keep walking, that is we require microscopic reversibility

$$P(\mathbf{m}_i|\mathbf{m}_j)\sigma_m(\mathbf{m}_j) = P(\mathbf{m}_j|\mathbf{m}_i)\sigma_m(\mathbf{m}_i). \quad (4.17)$$

From this and Eq. (4.13) we get

$$P(\mathbf{m}_i|\mathbf{m}_j)\rho_m(\mathbf{m}_j)L(\mathbf{m}_j) = P(\mathbf{m}_j|\mathbf{m}_i)\rho_m(\mathbf{m}_i)L(\mathbf{m}_i). \quad (4.18)$$

This requirement is met if we choose  $P(\mathbf{m}_j|\mathbf{m}_i)$  proportional to  $\rho_m(\mathbf{m}_j)L(\mathbf{m}_j)$  [Mosegaard, 1998].

Assume that we have a random walk that equilibrates at the a priori probability density  $\rho_m$ . We will now modify this random walk to sample the a posteriori probability density  $\sigma_m$  instead. As opposed to accepting every step suggested by the random walk and thereby sample the a priori probability density, we will sometimes discard the step and stay where we are. We will use the Metropolis criterion

$$P_{\text{accept}} = \min\left(1, \frac{L(\mathbf{m}_i)}{L(\mathbf{m}_j)}\right) \quad (4.19)$$

to decide whether or not to take the step from  $\mathbf{m}_j$  to  $\mathbf{m}_i$ : If the likelihood of the suggested model  $\mathbf{m}_i$  is higher than or equal to that of the current model  $\mathbf{m}_j$  the step is accepted. Otherwise the step is accepted with the probability  $\frac{L(\mathbf{m}_i)}{L(\mathbf{m}_j)}$ . It can be shown that this new random walk samples the a posteriori probability density [Mosegaard and Tarantola, 1995].

The specific random walk used in the inversion of the flow model, that simulates the flow in the area around NorthGRIP, is derived in Chapter 6.

## Chapter 5

# The Observed Data

In order to perform a Monte Carlo inversion of the flow model presented in Chapter 3, a set of known depth-age horizons is needed. As described in Section 2.2.3, the internal layers constitute such a set. The data used in this thesis is from a RES profile along the NNW-trending ice ridge from GRIP to NorthGRIP (see Fig. 5.1). The data were collected by the University of Kansas in 1999 [Chuah et al., 1996, Gogineni et al., 1998, Gogineni et al., 2001, Kanagaratnam et al., 2001]. The profile was measured with their coherent radar system, which operates at a center frequency of 150 MHz. The radar transmits a pulse with a duration of  $1.6 \mu\text{s}$  and a peak power of 200 W. The depth resolution in ice is 5 m and the horizontal resolution is 160 m [University of Kansas, RSL]. The system was operated from a NASA P-3 aircraft equipped with GPS receivers. Fig. 5.2 shows the radar image obtained along the ice ridge in 1999. It is seen from Fig. 5.1 that the RES profile does not run right past the NorthGRIP drill site, but passes it a few kilometres to the East. In 2003 the University of Kansas obtained a 19.3 km long RES profile that runs right past the drill site, and is parallel to the 1999 line. The radar image obtained along the 2003 line is seen in Fig. 5.3.

A comparison of the radar images from the two lines shows that though the overall structure of the layers is very similar in the two images, the layers are located up to several tens of meters deeper in the 2003 profile than in the 1999 profile (see Fig. 5.4). This is significant because the ss09sea depth-age relationship at NorthGRIP is used to date the fixpoints (the isochrones), and a difference in depth of several tens of meters corresponds to a significant difference in age. For the case of the lowest isochrone there is a difference of 25 m between the depth at the drill site and that at the point on the 1999 line, which is closest to it. This corresponds to an age difference of 1.8 kyr. To overcome this problem the 1999 line has been diverted towards

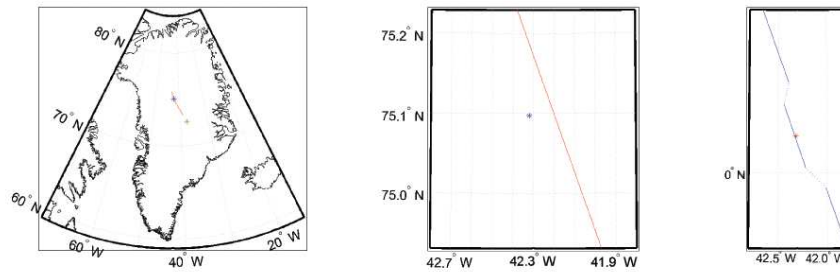


Figure 5.1: **Left:** The location of the 320 km long RES profile. The GRIP and NorthGRIP drill sites are marked by the green and blue asterisk, respectively. **Middle:** Close up of the figure to the left. Note that the profile does not pass right through NorthGRIP but passes a couple of kilometres East of the site. **Right:** The data line used in this study. The line has been diverted towards NorthGRIP. In the dotted parts of the line interpolated values have been used.

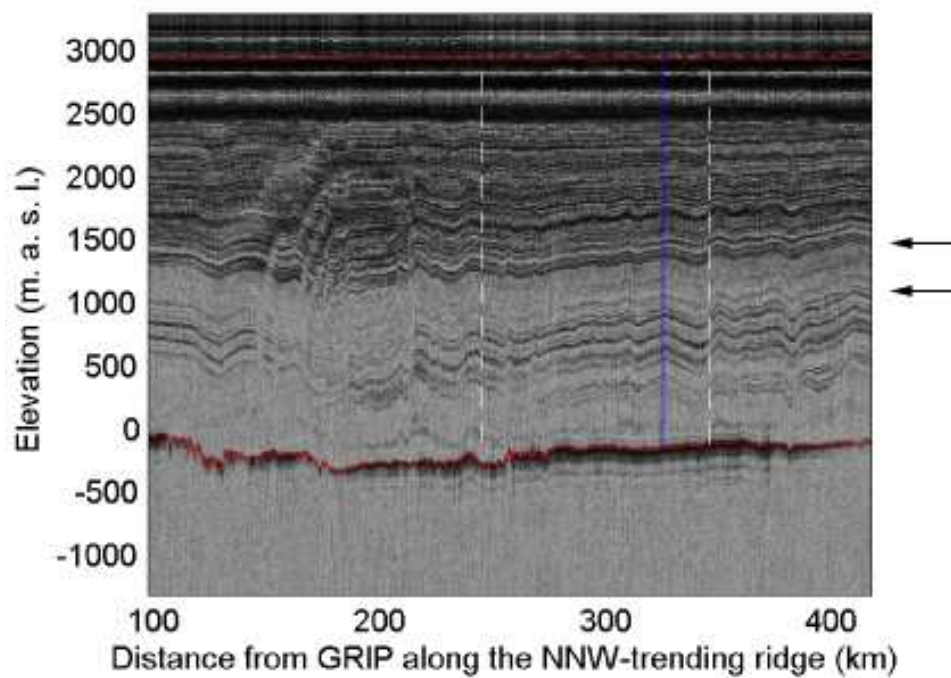


Figure 5.2: RES profile measured along the NNW-trending ice ridge from GRIP to NorthGRIP. The ice surface and the bedrock are marked in red. The NorthGRIP ice core is shown in blue and the dashed white lines indicate the beginning and the end of the 100 km long interval used in this work. The arrows to the right indicate a gap with weak or no reflectors. Data from [Chuah et al., 1996, Gogineni et al., 1998, Gogineni et al., 2001, Kanagaratnam et al., 2001].

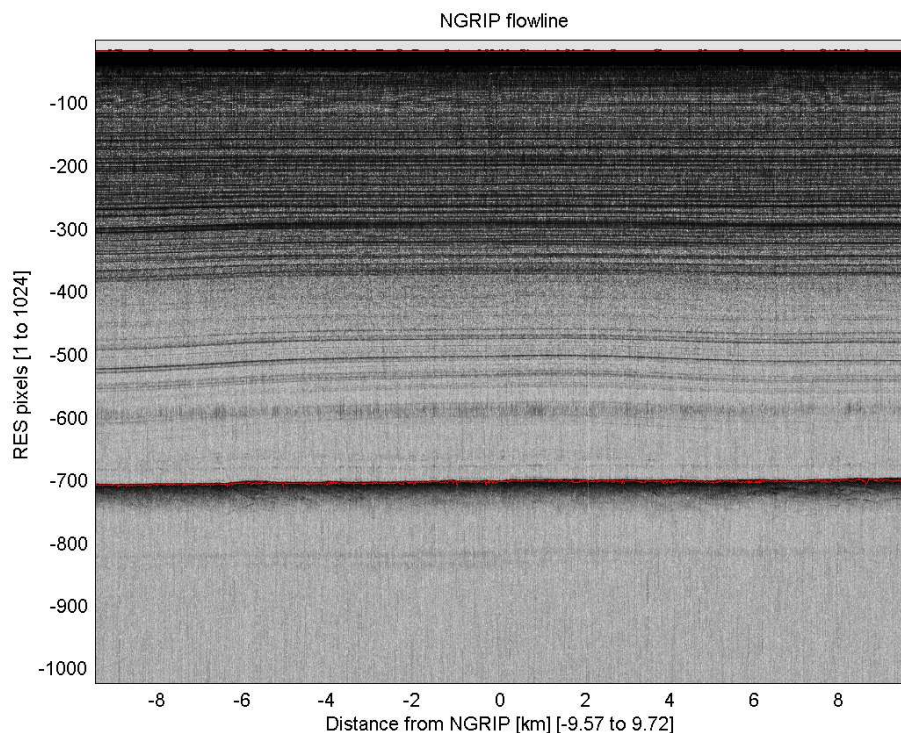


Figure 5.3: The 2003 RES profile that runs right past the NorthGRIP drill site. The drill site is located at  $x=0$ . The direction towards GRIP is to the left in the picture.

NorthGRIP in the vicinity of the drill site. This is done by replacing 19.3 km of 1999 data with the 2003 data in the vicinity of NorthGRIP. In each end of the replaced section a smooth interpolation between the two data sets is made over  $\sim 6$  km. The adopted data line is depicted on the right in Fig. 5.1.

Fig. 5.2 shows some prominent features. One is the gap with very weak or no reflectors found at NorthGRIP elevations of 900–1400 m. The gap is found in ice deposited around 20 kyr ago during the Last Glacial Maximum [Dahl-Jensen et al., 1997], and it is seen in most RES profiles from Greenland [Riishøjgaard, 1989]. The reason for the gap could be that the signals from volcanic eruptions are masked by the alkalinity of the ice from this period [Hempel et al., 2000]. Another important observation from Fig. 5.2 is that the layers are undulating along the line. The amplitude of the undulations is increasing with depth. This implies that the undulations can not be caused by accumulation variations along the line. Because the undulations have amplitudes of up to several hundred meters, bedrock topography also fails as a possible explanation. Most likely, the undulations are caused by changes in the basal melt rate along the line. The higher the melt rate is,

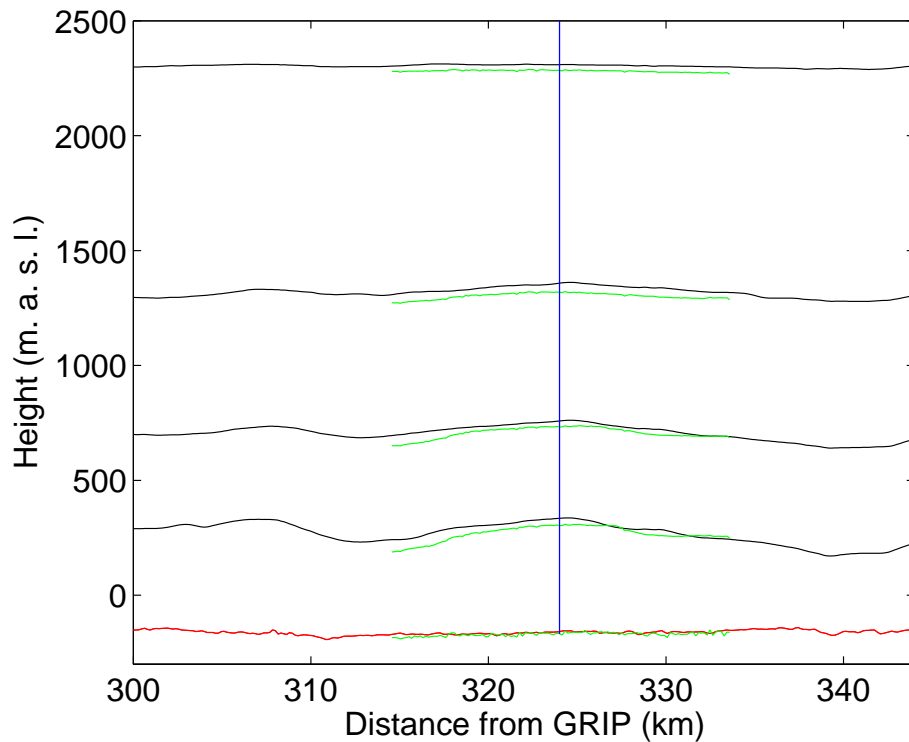


Figure 5.4: The depths of the isochrones in the 1999 profile (black) and in the 2003 profile (green). The bedrock is shown in red.

the further will the isochrones be dragged down. Notice that NorthGRIP is located at a spot where the isochrones are waving up. This site was chosen in order to have the Eemian ice located as far above bedrock as possible in the ice core [Dahl-Jensen et al., 1997]. About 200 km from GRIP a region of highly disturbed layers is seen. The disturbances are caused by very high melt rates [Fahnestock et al., 2001]. This is actually the region where the great ice stream covering most of North East Greenland has its offspring [Fahnestock et al., 2001].

## Chapter 6

# Inversion of the Flow Model

The system at hand is described by the modified Dansgaard-Johnsen model, its parameters, and the observed data presented above. This chapter describes the a priori information, explains the precise use of the data set, and gives an outline of the algorithm used for this specific problem.

### 6.1 A Priori Information

The a priori knowledge in the data space  $\mathcal{D}$  consists of the depths and ages of the internal layers (the data points) and the corresponding uncertainties. The model parameter vector is given by

$$\mathbf{m} = [c_1, c_2, \alpha, h_0, \beta, w_{b1}, w_{b2}, w_{b3}, \dots, w_{b13}]. \quad (6.1)$$

The a priori information on the model parameters consists of intervals that each parameter is confined to. The constraints on  $\alpha$  and  $h_0$  are given through  $h$  and those on  $\beta$  are given through  $F_B$  (cf. Eqs. (3.9) and (3.11)). The intervals are given in Table 6.1.

Parameter	Lower Boundary	Upper Boundary
$c_1$ ( $\%_{00}^{-1}$ )	0.04	0.3
$c_2$ ( $\%_{00}^{-1}$ )	0.04	0.3
$w_b$ (m/yr)	0	0.05
$h$ (m)	200	2800
$F_B$	0	1

Table 6.1: The intervals to which the values of the model parameters are confined. The constraints on  $\alpha$  and  $h_0$  are given through constraints on  $h$ , and those on  $\beta$  are given through constraints on  $F_B$ .

## 6.2 Choosing the Fix Points

As mentioned above the depths and ages of the ss09sea-dated isochrones constitute the observed data. It is seen from Fig. 5.2 that numerous isochrones can be distinguished on the RES images. Thus it is possible to create a vast data set from these images. However, if such a large data set is used in the search for the parameters of the flow model, the system would be completely tied to the ss09sea dating, and only a minimal amount of new information would be gained from the present analysis. Thus we will choose a number of data points that is sufficient to gain information on the model parameters, but not so large that the analysis is tied too strictly to the ss09sea dating. I have decided to use five fix points for the inversion, four of which are given depth-age relationships. The first three are constituted by the isochrones ss09sea-dated to 3.6, 14.6, and 45.8 kyr BP (BP here meaning before 2000 A.D.). These layers have been carefully selected according to the following criteria:

- The data set must contain points from the Holocene as well as the glacial period.
- The layers must be easily distinguishable from the surrounding layers in the RES images.

The Holocene and glacial periods are represented by the 3.6 kyr and the 45.8 kyr isochrones, respectively. The 14.6 kyr isochrones marks the onset of the Bølling interstadial.<sup>1</sup> These three isochrones are indicated on the

<sup>1</sup>An interstadial is a relatively short-lived period with thermal improvement during a glacial period. 25 interstadials have been observed in Greenland during the past glacial period. Bølling constitutes Greenland Interstadial 1.

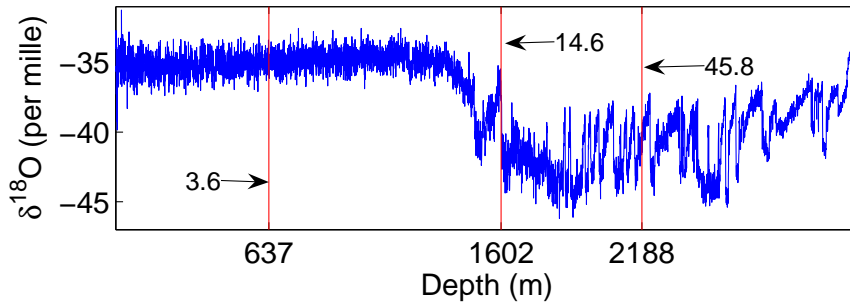


Figure 6.1: The depths of the chosen isochrones are indicated on the  $\delta^{18}\text{O}$  curve. The ss09sea age in kyr BP is indicated for each isochrone.

$\delta^{18}\text{O}$  curve on Fig. 6.1 and they are shown as solid white lines on the radar image in Fig. 6.2. The fourth depth-age fix point is the age at the bottom at NorthGRIP. This fix point is indicated by the white asterisk in Fig. 6.2. Finally, a fifth fix point with no constraints regarding the dating is introduced: A weak isochrone near bedrock is visible in the radar images, and the shape of this layer is used to further constrain the analysis. Strictly speaking, this fifth fix point is not a data point since it does not relate depth and age. However, it is a good way to constrain our analysis: If the shape of a modelled layer at this depth (regardless of the age) does not resemble that of the observed isochron, the values used for the model parameters can not be good estimates. This lower isochrone is shown as the dashed white line in Fig. 6.2.

### 6.3 Accounting for Uncertainties

The uncertainty on the depth of an isochrone is a result of the limited resolution of the radar used to recover the data. This uncertainty is accounted for through the likelihood function, Eq. (4.15). However, there is also an uncertainty on the dating of the ice core. This is accounted for by calculating two misfits for the depth-age fix points – one for the depth (the shape) of the isochrone and one for the age. The fix points and the uncertainties are given in Table 6.3.

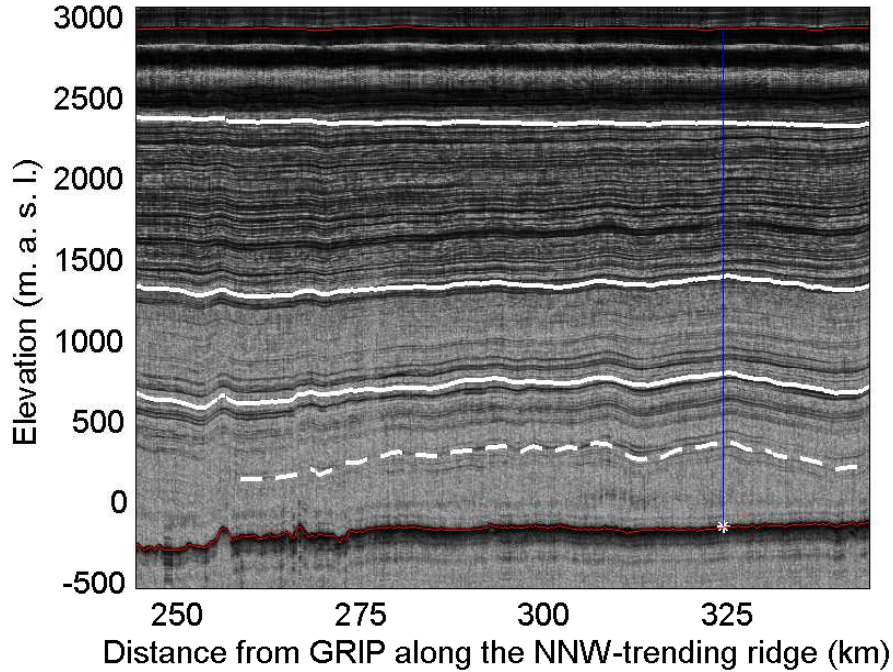


Figure 6.2: The section of the 1999 RES profile used in the present study. The three solid white lines indicate the isochrones of ages 3.6 kyr, 14.6 kyr, and 45.8 kyr. These are used as fixed depth-age horizons in the Monte Carlo inversion. The dashed white line indicates the deep layer used to further constrain the model. Only the shape of this layer is regarded in the analysis – no fixed age has been assigned to it. Finally, the age at the bottom at NorthGRIP is used as a fix point. This is indicated by the white asterisk.

Fix point	Depth at NGRIP	ss09sea-age
Holocene Isochrone	$637 \pm 10$ m	$3.6 \pm 0.05$ kyr
Bølling Isochrone	$1602 \pm 10$ m	$14.6 \pm 0.5$ kyr
Glacial kyr Isochrone	$2188 \pm 10$ m	$45.8 \pm 2$ kyr
Lower Isochrone	$2617 \pm 10$ m	Not used
Bottom	$3085 \pm 10$ m	$123 \pm 2$ kyr

Table 6.2: The depths and ss09sea-ages of the selected fix points.

## 6.4 Creating the Random Walk

As the a priori information on the model parameters only consists of an interval for each parameter, it is straight forward to construct a random walk that samples the a priori probability density  $\rho_m$  in the model space.

It merely has to pick each value in the interval with equal probability. By accepting or rejecting the suggested step using the Metropolis criterion from Eq. (4.19) this walk is modified to sample the a posteriori probability density  $\sigma_m$  instead. In every step each model parameter is altered by a uniformly distributed random value. The maximum change in value is given by a step length for each parameter. The step lengths are chosen in order to get a reasonable acceptance rate for the random walk. If the step length is chosen too small the search of the model space will proceed very slowly, and if it is chosen too big a large number of steps will be rejected. As the misfit gets smaller the step length is gradually reduced in order to maintain the acceptance rate. The initial step lengths are shown in Table 6.3.

Parameter	$c_1$ ( $\%_{00}^{-1}$ )	$c_2$ ( $\%_{00}^{-1}$ )	$\alpha$ (yr)	$h_0$ (m)	$\beta$ (yr/m)	$w_b$ (m/yr)
Step Length	0.002	0.002	1000	100	1	0.001

Table 6.3: The initial step lengths for the model parameters.

Now we have all the tools we need to solve the problem. The algorithm is outlined below:

1. Make a guess as to the values of  $\mathbf{m}$
2. Run the forward model
3. Calculate the misfit  $S(\mathbf{m})$
4. Perturb the model  $\mathbf{m} \longrightarrow \mathbf{m}_{\text{test}}$
5. Run the forward model with the perturbed model parameters  $\mathbf{m}_{\text{test}}$
6. Calculate the new misfit  $S(\mathbf{m}_{\text{test}})$
7. Accept or reject the perturbed model according to the Metropolis criterion.
8. Repeat from step 4

Every time the forward model is run, a modelled isochrone is followed as it sinks down through the ice sheet. The better this modelled isochrone matches the shapes and ages of the observed isochrones, the smaller is the misfit. The accepted model parameters are stored, and after sufficiently many steps by the random walk, the set of accepted model parameters

---

represent the a posteriori probability density. The random walk must be continued until there is no trend in the misfit, and doubling the number of accepted models will not change the histograms for the accepted model parameters significantly. The mean of all the accepted values of a model parameter can then be regarded as a posterior-probability weighted mean. Running the forward model with these mean values for the parameters will result in the desired timescale (the relation between depth and age).

Because the ss09sea-dated  $\delta^{18}\text{O}$  curve is used to obtain the accumulation history at NorthGRIP, the derived timescale will inevitably depend on the ss09sea dating. In order to minimize this dependence a second Monte Carlo inversion of the flow model is performed. In this second inversion the timescale derived from the results of the the inversion is used instead of the ss09sea timescale to calculate the accumulation history and to date the fix points. The results from the second inversion are presented in the next chapter.

# Chapter 7

## Results and Discussion

### 7.1 The Model Parameters

#### 7.1.1 The Basal Melt Rate, $w_b$

As described in Section 3.2 the 100 km long section of the ice ridge between GRIP and NorthGRIP investigated in this study was divided into 13 intervals of 8 km (except the very first interval which is only 4 km). The melt rate was assumed to be constant within each of these intervals. The Monte Carlo inversion reveals estimates of the melt rates in the intervals. Because the effect of basal melting increases with depth, the deep fix points are very important for the determination of the melt rate. At a depth of  $\sim 2$  km the modelled isochrone has typically moved  $\sim 20$  km along the ridge, and thus left the three first melt rate intervals (see Fig. 7.3). This means that the inversion has not had any constraints in the deep part of the ice for the first 20 km of the line, and the melt rate estimates obtained for that area can not be considered reliable. Fig. 7.1 shows histograms of the accepted melt rates in the remaining 10 intervals. All these histograms show strong single maxima, which indicates that the melt rates in these intervals are well determined by the inversion. The variation of the melt rate along the line is depicted in the upper panel of Fig. 7.2. The values vary between  $4.1 \pm 0.5$  mm/yr and  $10.4 \pm 1.1$  mm/yr. The lowest value along the line is found at NorthGRIP.

In the vicinity of NorthGRIP the line of data was diverted towards the drill site (cf. Chapter 5). In the zone 308–315 km from GRIP the used depths of the isochrones are interpolations between the 1999 and 2003 profiles (cf. Fig. 5.1). Upstream from NorthGRIP the isochrones are located up to several tens of meters deeper in the 2003 profile than in the 1999

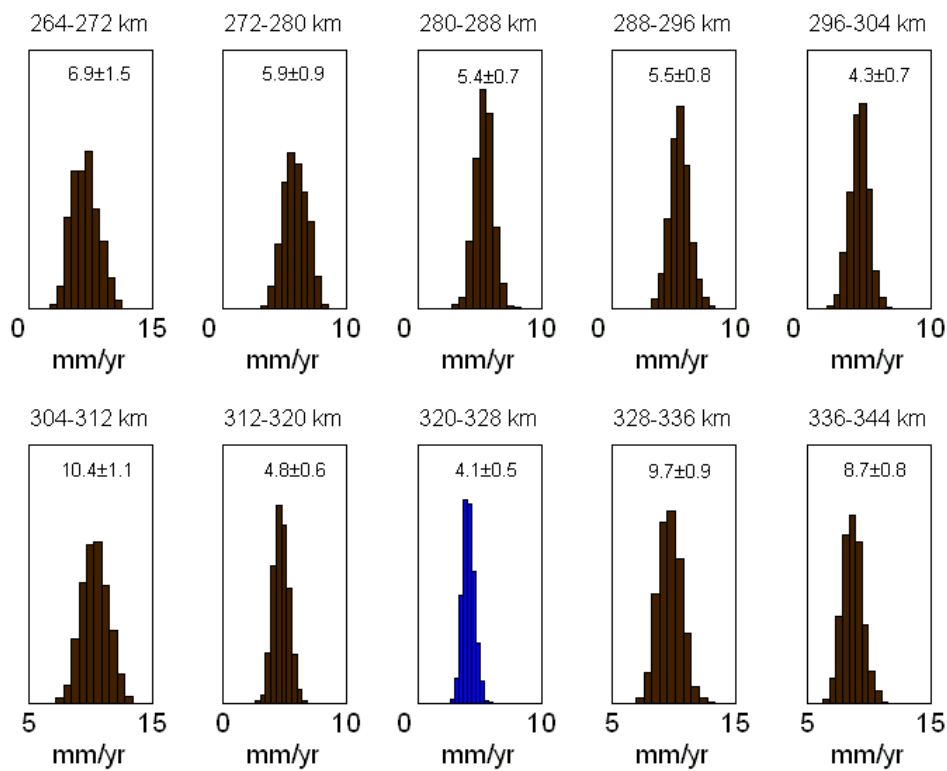


Figure 7.1: The a posteriori probability distributions for the melt rates in the last 10 intervals along the line. The distance from GRIP is given above each histogram. The histogram for the interval containing NorthGRIP is shown in blue. The mean value and standard deviation are given above each distribution.

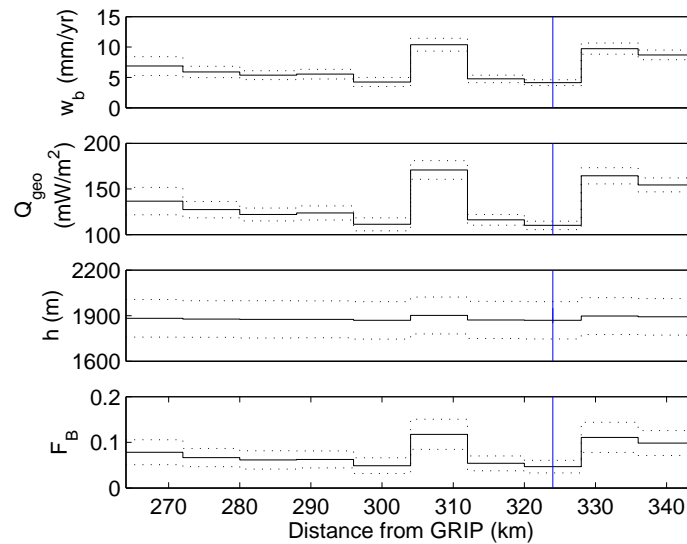


Figure 7.2: From the top: Melt rate, geothermal heat flux, kink height, and bottom sliding along the flow line. The solid line is the mean value of the parameter, and the dotted lines represent one standard deviation to either side of the mean value. The blue line indicates the position of NorthGRIP.

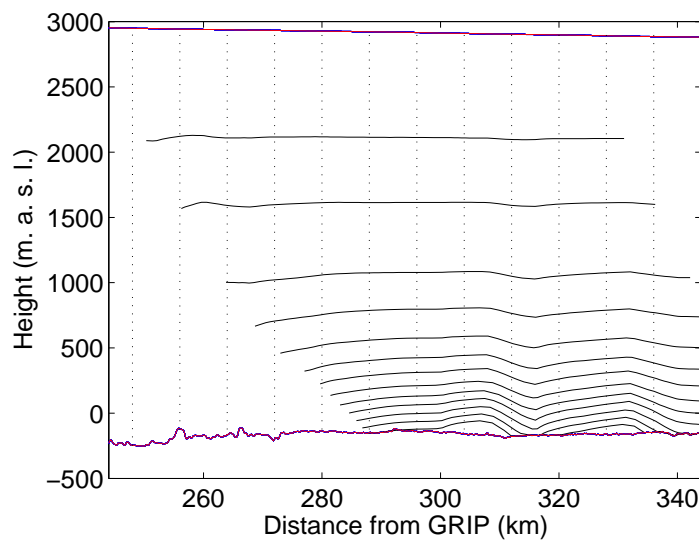


Figure 7.3: The solid black lines indicate the modelled isochrone at different times. The surface and bottom of the ice are marked in red. The dotted lines indicate the melt rate intervals. It is seen that the modelled isochrone has left the first three intervals before it reaches large depths.

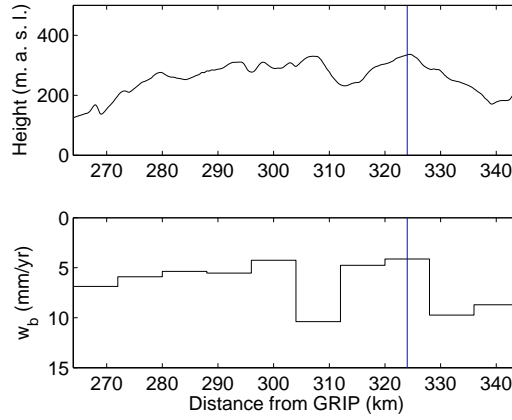


Figure 7.4: Above: The lowest isochrone from the radar data set used in this study. Below: The melt rates along the line found from the Monte Carlo inversion. Notice the reversed vertical axis. NorthGRIP is indicated by the blue line.

profile. Consequently, an artificial contribution to the dip of the isochrones is created in the interpolation zone. Thus we expect the melt rate found for the intervals 304–312 km and 312–320 km to be somewhat overestimated. In the interpolation zone downstream from NorthGRIP (334–340 km) the differences between the depths of the deep isochrones in the two profiles are of the order of a few meters (see Fig. 5.4), and the moving of the flow line is not believed to have had a significant effect on the obtained melt rates in this area.

Fig. 7.4 shows a comparison between the shape of the lowest isochrone and the variation of the melt rate along the line – notice the reversed vertical axis for the melt rate plot. The two curves show very similar patterns, but the isochrone curve is shifted a little bit to the right. The shift can be explained by the horizontal flow velocity of the ice. The features created by the melt rate at a given place is carried with the ice along the line. The observations from Fig. 7.4 support the assumption that the shape of the isochrones is related to variations in the melt rate.

When the melt rate is known, the amount of heat used to melt the ice,  $Q_{\text{melt}}$ , can be calculated using the relation

$$Q_{\text{melt}} = \rho w_b L, \quad (7.1)$$

where  $\rho$  and  $L$  are the density and the latent heat of the ice, respectively. The amount of heat transported through the ice at the base,  $Q_{\text{ice}}$ , is given by

$$Q_{\text{ice}} = -K \frac{\partial T}{\partial z}, \quad (7.2)$$

where  $K$  is the thermal conductivity of ice, and  $\frac{\partial T}{\partial z}$  is the temperature gradient at the base. Using  $Q_{\text{ice}}=70 \text{ mW/m}^2$  [North Greenland Ice Core Project Members, 2004] and the basal melt rates found in this study, the geothermal heat flux  $Q_{\text{geo}}$  along the line is calculated from the relation

$$Q_{\text{geo}} = Q_{\text{melt}} + Q_{\text{ice}}. \quad (7.3)$$

The obtained values are between  $110\pm 5 \text{ mW/m}^2$  and  $171\pm 10 \text{ mW/m}^2$  (see Fig. 7.2). The lowest value is found at NorthGRIP. As the geothermal heat flux is calculated from the obtained melt rates we expect a positive artificial contribution to the geothermal heat flux in the 304–312 km and 312–320 km intervals. The geothermal heat flux in the NorthGRIP area is considerably larger than that at GRIP. At GRIP there is no basal melt and the geothermal heat flux can be calculated directly from the observed temperature gradient at the base. This reveals a value of  $51 \text{ mW/m}^2$  [Dahl-Jensen et al., 1998], which is a typical value for Precambrian shield, that is believed to cover most of Greenland. The high values of  $Q_{\text{geo}}$  found in this study are atypical for Precambrian shield.

### 7.1.2 The Kink Height, $h$

Fig. 7.5 shows the a posteriori probability distribution for the remaining five model parameters. The kink height  $h$  was tied linearly to the melt rate, with using the parameters  $\alpha$  and  $h_0$  (cf. Eq. (3.9)). The distribution for  $h_0$  shows a strong single maximum at  $1848\pm 128 \text{ m}$ , while the value of  $\alpha$  is not well determined by the inversion, since the uncertainty is of the same order as the value itself (see Fig. 7.5). However, if we for each set of accepted model parameters calculate the value of  $h$  from Eq. (3.9), the distributions of  $h$  for each melt rate interval all show a strong single maximum. Because the contribution to  $h$  from  $h_0$  is considerably larger than that from  $\alpha$  and  $w_b$ , the ill determined nature of  $\alpha$  has little effect on the value of  $h$ . The histogram for  $h$  for the interval containing NorthGRIP is shown in Fig. 7.6. The obtained values of  $h$  are between  $1869\pm 123 \text{ m}$  and  $1902\pm 121 \text{ m}$  (see Fig. 7.2). The artificially high melt rate in the interpolation zone may lead to an artificially high value of  $h$  in that area, but as the effect of the melt rate on  $h$  is little, the overestimation is believed to be small.

### 7.1.3 The Fraction of Basal Sliding, $F_B$

The mean value of  $\beta$  is  $11.5\pm 3.6 \text{ yr/m}$ , but the histogram shows two separate maxima at  $8.2 \text{ yr/m}$  and  $13.9 \text{ yr/m}$  (see Fig. 7.5). Because  $F_B$  is calculated from  $\beta$  using Eq. (3.11) the ambiguity in  $\beta$  might be present in  $F_B$  also.

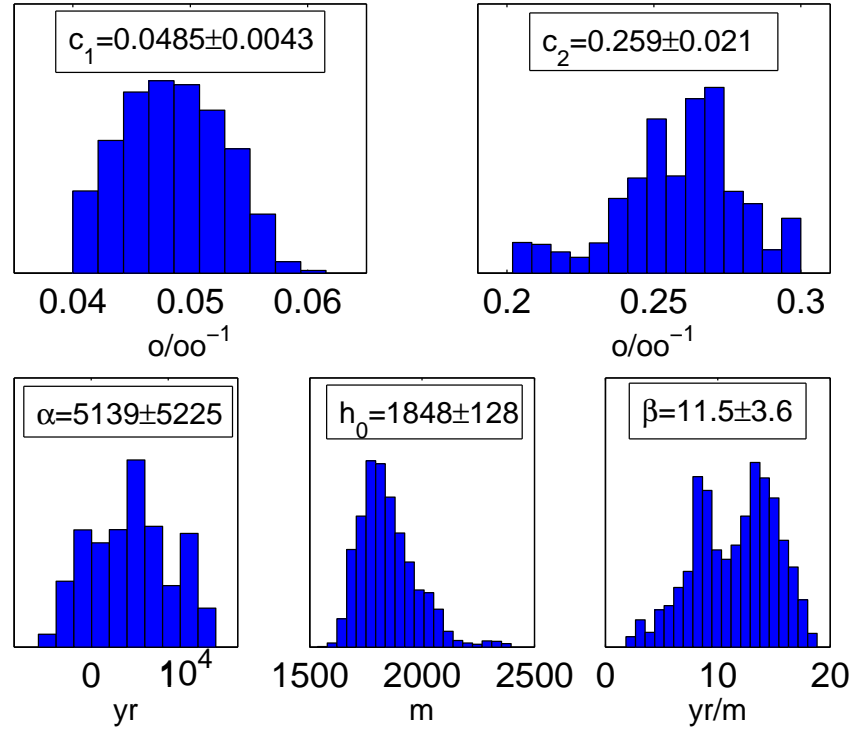


Figure 7.5: The a posteriori probability distributions for the model parameters. The mean and standard deviation for each parameter is given above the distribution.  $c_1$  and  $c_2$  are the parameters of the accumulation model, while  $\alpha$  and  $h_0$  are used to calculate the kink height  $h$  from the melt rate.  $\beta$  links the fraction of bottom sliding,  $F_B$ , to the melt rate.

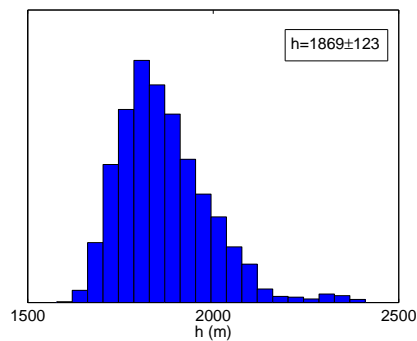


Figure 7.6: The histogram for the values of  $h$  for the interval containing NorthGRIP (320–328 km). The histograms for the other intervals along the line look very similar.

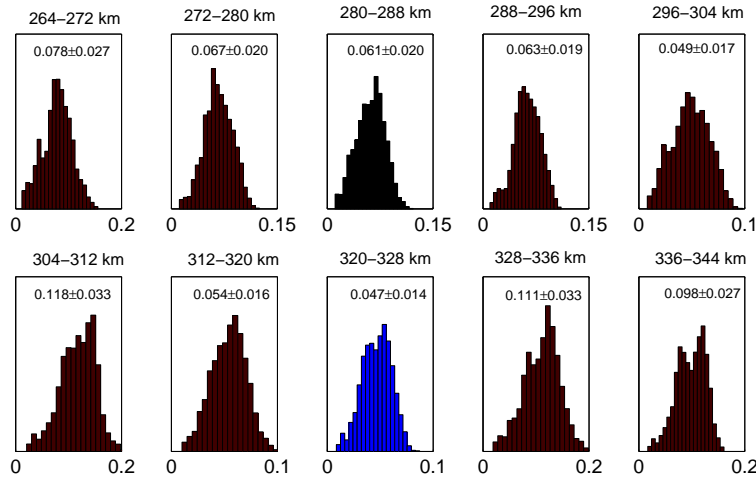


Figure 7.7: The histograms for the calculated values of  $F_B$  along the line. The mean value and standard deviation are given above each distribution, and the distance of the melt rate interval from GRIP is indicated above each plot. The Interval containing NorthGRIP is shown in blue. It is seen that the histograms for the last three intervals have double peaks.

The histograms for the values of  $F_B$  for each melt rate intervals show, that this is mainly the case for the last three intervals (see Fig 7.7). Thus the ambiguity is only present downstream from the drill site, and has therefore not affected the dating of the core. The obtained values for  $F_B$  vary between  $0.047 \pm 0.014$  and  $0.118 \pm 0.033$  along the line (see Fig. 7.2). As for the case of  $h$  the artifact from the melt rate in intervals 304–312 km and 312–320 km may cause an overestimation of the fraction of sliding in this interval.

#### 7.1.4 The Accumulation History

The parameters  $c_1$  and  $c_2$  of the accumulation model are estimated to  $0.0485 \pm 0.0043 \text{ } \text{‰}^{-1}$  and  $0.259 \pm 0.021 \text{ } \text{‰}^{-1}$ , respectively, but the histogram for  $c_2$  is not very smooth (see Fig. 7.5). The resulting accumulation history for NorthGRIP is shown in Fig. 7.8. The mean accumulation rate in the Holocene is found to be 0.199 m/yr, which is close to the observed 0.193 m/yr. According to the obtained accumulation history for NorthGRIP, the accumulation rate was as low as 0.05 m/yr during the Last Glacial Maximum 20 kyr ago (the coldest part of the glacial period). This value is only 25 % of the Holocene value. This large temporal variation in the accumulation rate illustrates the importance of using a time dependent accumulation model when establishing a timescale for the NorthGRIP ice core.

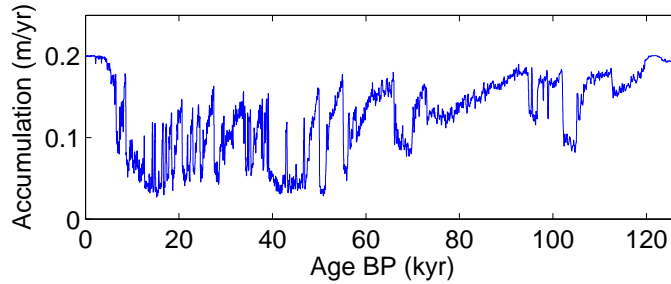


Figure 7.8: The accumulation history for NorthGRIP calculated with  $c_1=0.0485 \text{ } \text{‰}^{-1}$  and  $c_2=0.259 \text{ } \text{‰}^{-1}$ .

## 7.2 Correlation Between the Parameters

The system at hand is highly non-linear and correlations between the parameters are expected. The correlation matrix is plotted in Fig. 7.9. It is seen that the strongest correlation is between  $c_1$  and  $c_2$ . The correlation coefficient is calculated to 0.77. This strong correlation suggests that the same information is contained in the two parameters. Therefore one could consider eliminating one of the parameters in the accumulation model and thus having one less parameter to determine. In this study, however, both parameters were used. A scatter plot of the accepted values of  $c_1$  and  $c_2$  is found in Fig. 7.10. The points are seen to fall close to a straight line.

$c_2$  and  $h_0$  are negatively correlated with a correlation coefficient of -0.37. The correlation between the two parameters can be understood by considering the effects of the accumulation rate (represented by  $c_2$ ) and the kink height (represented by  $h_0$ ) on the layer thickness profile. A decrease in  $c_2$  causes an increase in the accumulation rate for most of the period, and increased accumulation leads to higher layer thicknesses. An increase in  $h_0$  corresponds to an increase in  $h$ , which leads to thinner layers. Thus changing  $c_2$  and  $h_0$  in opposite directions maintains the layer thickness profile.

## 7.3 The New Timescale

A new timescale for the NorthGRIP ice core is established by running the forward model with the parameters obtained from the second Monte Carlo inversion. Fig. 7.11 shows the depth-age relationship found from the first inversion in green and that from the second inversion in blue. The depth-age relationship from the ss09sea timescale is shown in red for comparison. Fig. 7.12 shows the  $\delta^{18}\text{O}$  curve plotted on ss09sea timescale (red) and on the timescale obtained in this study (blue). It is seen that the new timescale

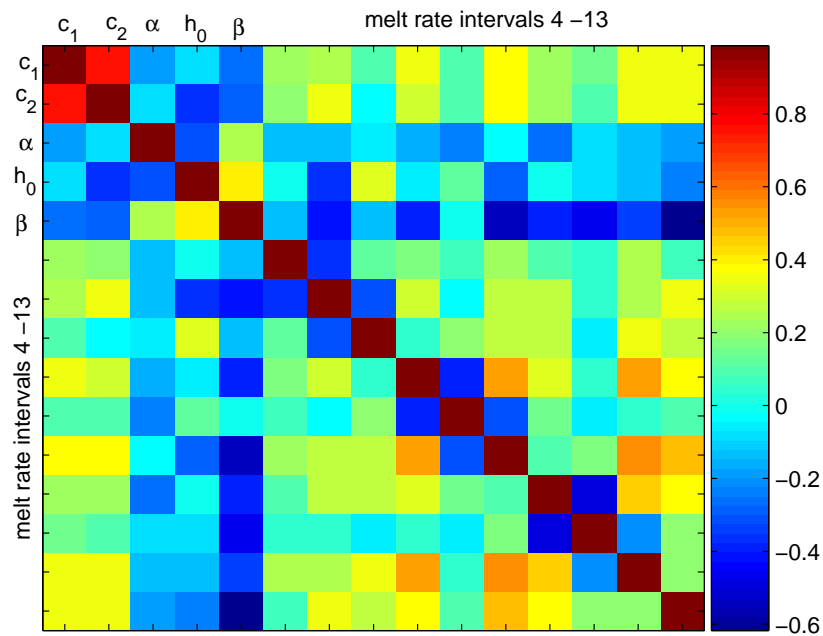


Figure 7.9: The correlations between the model parameters. Dark red colours correspond to positive correlations, while dark blue colours correspond to negative correlations.

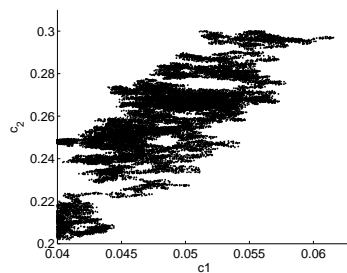


Figure 7.10:  $c_1$  vs.  $c_2$ . A strong positive correlation is observed. The correlation coefficient can be calculated to 0.77.

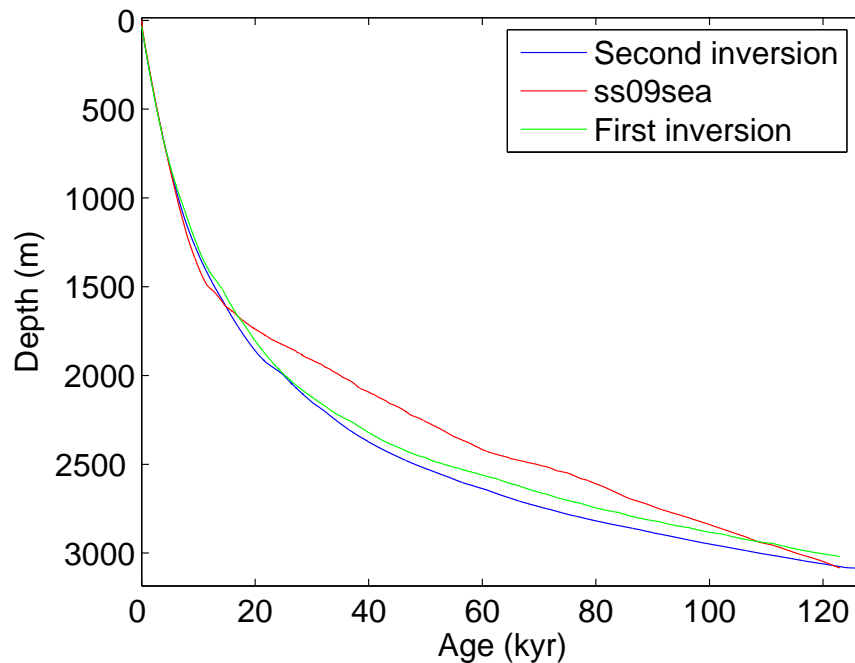


Figure 7.11: The depth-age relationship from the first (green) and the second (blue) inversion of the flow model presented in Chapter 3. The red curve shows the ss09sea timescale for comparison.

assigns younger ages to the glacial period and older ages to the Eemian period compared to the ss09sea timescale. The new timescale assigns an age of 126.5 kyr to the bottom of the core. This is 3.5 kyr older than the ss09sea age of 123 kyr. The new dating indicates a slower transition from the warm Eemian temperatures to the cooler intermediate temperatures reached just before the onset of Greenland Interstadial 25. According to the ss09sea timescale this transition takes seven kyr, but according to the new timescale it takes 12 kyr. The older dating of the bottom ice indicates that the core contains a larger part of the Eemian than previously assumed.

Fig. 7.13 shows the trajectories of ice found at the depths of the fix points in NorthGRIP ice core. The ice at the bottom at NorthGRIP has travelled a horizontal distance of 48 km. This ice was deposited 276 km from GRIP, which is well within the 100 km section treated in this study. The unreliable melt rate estimates for the first 20 km of the section is therefore not believed to have affected the timescale derived for the NorthGRIP ice core.

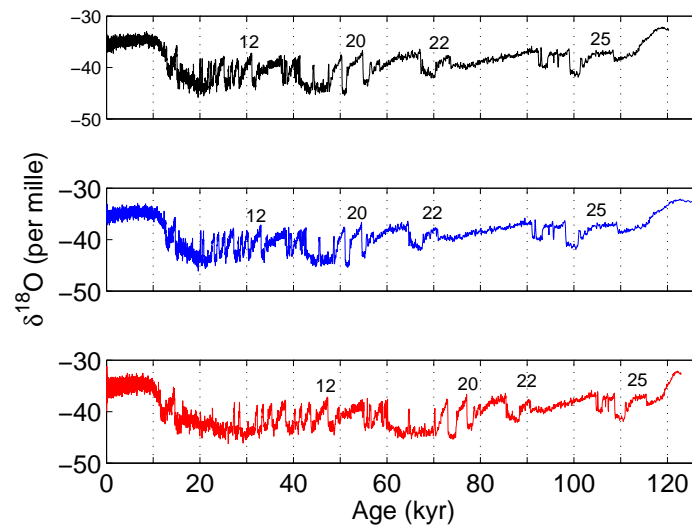


Figure 7.12: The NorthGRIP  $\delta^{18}\text{O}$  curve in 50 years resolution plotted on the ss09sea timescale (red), on the timescale found from the present two-dimensional study (blue), and the timescale from the one-dimensional version of the model presented in this study (black). A few of the Greenland Interstadials are indicated to make the comparison of the curves easier.

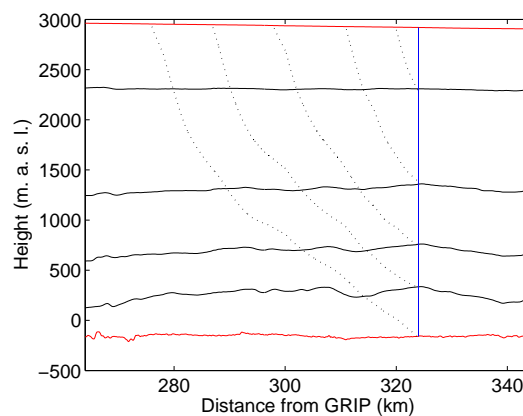


Figure 7.13: The travel paths (dotted lines) of the ice presently found at depths of 637 m, 1602 m, 2188 m, 2617 m, and 3085 m at NorthGRIP. The basal ice has travelled a horizontal distance of 48 km. The isochrones used to constrain the Monte Carlo inversion are shown as solid lines. The NorthGRIP ice core is indicated in blue and the surface and the bedrock in red.

## 7.4 Discussion of Assumptions

The accumulation rate model is built on the assumption that a positive correlation exists between the accumulation and the  $\delta^{18}\text{O}$  values. This assumption is supported by observations from Central Greenland: Dahl-Jensen et al. [1993] found a strong positive correlation between past accumulation rates and  $\delta^{18}\text{O}$  values at the GRIP site.

The ratio between the accumulation rate at NorthGRIP and that at other locations along the flow line was assumed constant in time. At present the ratio of the accumulation at NorthGRIP to that at GRIP is 83 %, but Grinsted and Dahl-Jensen [2002] found that this ratio was as low as 66 % during the glacial period. This indicates that the accumulation ratio at other places along the line may also have changed in time. Consequently the assumption of unchanged accumulation pattern along the line during time may be poor. The results from Grinsted and Dahl-Jensen [2002] indicate that the accumulation pattern seen today in the area between GRIP and NorthGRIP was more pronounced during the glacial period. If this is the case, the accumulation rates used upstream from NorthGRIP in this model are slightly overestimated for the glacial period. An overestimation of the accumulation rate leads to overestimated vertical velocities and consequently younger ages with depth.

By comparing the climate records from cores from different sites in Greenland North Greenland Ice Core Project members [2004] find that the ice thickness in Northern Greenland during the Eemian was within 100 m of the current thickness. Furthermore, Letréguilly et al. [1991] used a three-dimensional time-dependent ice sheet model to simulate the evolution of the Greenland Ice Sheet during the last 150 kyr, and they found that the ice thickness in Central Greenland was almost unchanged during this period. Thus the assumption of constant ice thickness in time seems reasonable.

The melt rate was also assumed to be constant in time. However, the temperature at a given depth in the ice cap depends on the surface temperature at the time the layer was formed (cf. Section 2.1.2). This and the changing accumulation cause the advection of cold ice to the bottom to change with time. The geothermal heat flux does not change considerably on this timescale. Therefore the melt rate will change in time (cf. Eq. (7.3)). The temporal variation of the melt rate could be accounted for by using a thermo-mechanical model, but incorporating this into the Monte Carlo inversion would make the computations too slow.

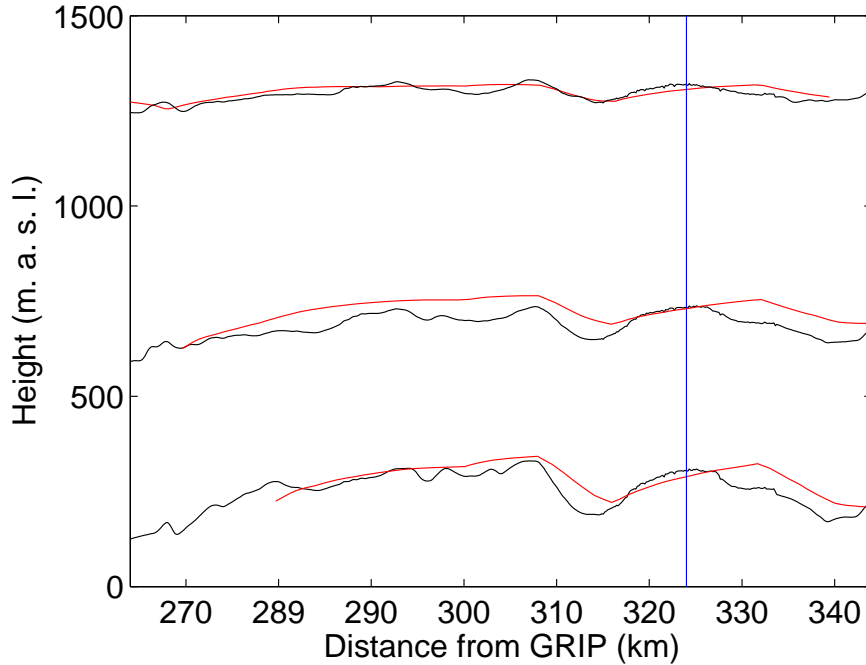


Figure 7.14: Observed (black) and modelled (red) isochrones. The modelled isochrones reproduce the large scale undulations of the observed isochrones.

## 7.5 Comparison With Observations

The modelled isochrones are shown together with the observed ones in Fig. 7.14. It is seen that the modelled isochrones capture the large scale wickles of the observed isochrones. The 8 km resolution in the melt rate makes it impossible for the model to capture the small scale undulations. It is concluded that the model is able to reproduce the observed data well.

## 7.6 The One-Dimensional Model

By disregarding the horizontal velocity component the two-dimensional model presented in Chapter 3 is reduced to a one-dimensional model. The computation time is significantly shorter for the one-dimensional model. By comparing the results from the inversions of the one- and two-dimensional models, the advantages of the two-dimensional model may become apparent.

The results of the inversion of the one-dimensional version of the model is seen in Fig. 7.15. No well defined values are found for  $c_1$  and  $c_2$ , but  $c_1$  is very

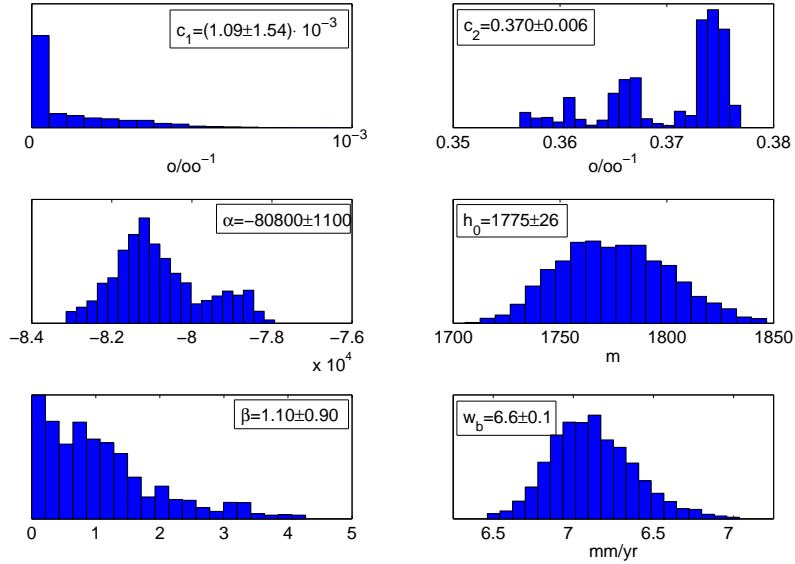


Figure 7.15: The histograms for the accepted model parameters for the one-dimensional model.

close to zero and  $c_2$  tends to be larger than the result for the two-dimensional model. The resulting accumulation rates during the Last Glacial Maximum are as low as 0.02 m, which is highly unlikely. This unrealistic accumulation history is a result of not taking the upstream effects into account.

The melt rate is found to be  $6.6 \pm 0.1$  mm/yr, which is close to the mean of the melt rates obtained along the line with the two-dimensional model. The timescales from the one- and two-dimensional models are very similar, but close to the bottom there are significant differences (see Fig. 7.16). The one-dimensional model dates the bottom ice to 121 kyr BP – 5.5 kyr younger than the two-dimensional model. This younger age at the bottom is caused by the higher melt rate at NorthGRIP.

The  $\delta^{18}O$  curve is plotted in black on the timescale from the one-dimensional model in Fig. 7.12. The transition from the warmest of the Eemian to the onset of Greenland Interstadial 25 takes 10 kyr.

Even though the differences between the timescales from the one- and two-dimensional models are smaller than I had anticipated I believe it is worth taking the extra trouble to use the two-dimensional model. Especially for the bottom part of the core the results from the two-dimensional model are more reliable, because the ice found here has travelled the longest horizontal distance (cf. Fig. 7.13). Furthermore, the inversion of the two-dimensional

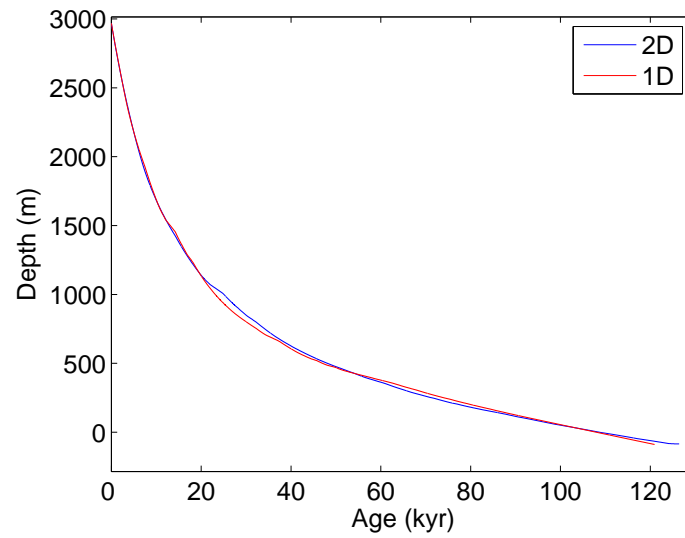


Figure 7.16: The depth-age relationship found from inversion of the 2-dimensional model (blue) and the 1 dimensional version (red), respectively.

model gives knowledge on the conditions in the area, e.g. estimates of the variation of the melt rate along the line.

## Chapter 8

# Conclusion

A modified Dansgaard-Johnsen model was used to simulate the flow along a 100 km section of the ice ridge between GRIP and NorthGRIP. The flow model was successfully inverted using a Monte Carlo method. This revealed estimates for 18 input parameters. Disregarding the first 20 km of the section where the inversion was insufficiently constrained, the parameters were generally well determined by the inversion.

The melt rate at NorthGRIP was estimated to  $4.1 \pm 0.5$  mm/yr. As expected, the melt rate was found to vary along the line of investigation. The wickles of the deep isochrones were found to follow the melt rate pattern, but the features were shifted along the ridge. This can be explained by the ice flowing along the ridge. The ice at the bottom was found to have been deposited 48 km upstream from the drill site.

The geothermal heat flux was determined to  $110 \pm 5$  mW/m<sup>2</sup> at NorthGRIP. Both upstream and downstream from the site the value is higher.

A new timescale for the NorthGRIP ice core was established from the estimated parameters. This new timescale assigns an age of 126.5 kyr to the ice at the bottom – 3.5 kyr older than the ss09sea age. It predicts a much slower temperature decline at the end of the Eemian period than the ss09sea model (12 kyr compared to 7 kyr).

A one-dimensional version of the flow model was also inverted. The resulting timescale was surprisingly similar to that obtained by the two-dimensional model, but the accumulation history obtained from the one-dimensional model showed unrealistically low accumulation rates during the glacial. This is the result of not accounting for the change in conditions upstream from the drill site. The two-dimensional model is believed to provide more reliable results – especially in the deep part of the core.

The advantage of the new model compared to the ss09sea model is that it accounts for the enhanced melting upstream from the drill site. It should be emphasized that this model was developed with the purpose of dating the ice found deep in the NorthGRIP ice core.

## Chapter 9

# Outlook

An obvious next step would be to improve the model by allowing several parameters and not just the accumulation rate to vary with time. Accounting for the temporal changes in melt rate and accumulation pattern along the line would raise the credibility of the model results.

In the lower part of the ice sheet the ice is strongly anisotropic, which affects the flow significantly. The fabric at a given depth can be determined from studying thin sections from the ice core under crossed polaroids. The model presented in this thesis may be modified to account for the change of fabric with depth.

The shape of the deep isochrones was seen to follow the melt rate pattern. That indicates that the shape of the isochrones as seen on the radar images can be used to infer the amount of melt under the ice in Greenland. This would contribute significantly to the understanding of the mass balance of the Greenland Ice Sheet.

# Bibliography

- [Azuma, 1994] Azuma, N. (1994). A flow law for anisotropic ice and its application to ice sheets. *Earth and Planetary Science Letters*, 128:601–614.
- [Bogorodsky et al., 1985] Bogorodsky, V. V., Bentley, C. R., and Gudmandsen, P. E. (1985). *Radioglaciology*. D. Reidel Publishing Company.
- [Chuah et al., 1996] Chuah, T. S., Gogineni, S. P., Allen, C., and Wohletz, B. (1996). Radar thickness measurements over the Northern part of the Greenland ice sheet. Technical Report 10470-3, Lawrence, KS, University of Kansas Center for Research Inc. Radar Systems and Remote Sensing Laboratory.
- [Clough, 1977] Clough, J. W. (1977). Reflections from internal layers in ice sheets. *Journal of Glaciology*, 18(78):3–14.
- [Dahl-Jensen et al., 2003] Dahl-Jensen, D., Gundestrup, N. S., Gogineni, P., and Miller, H. (2003). Basal melt at NorthGRIP modeled from borehole, ice-core and radio-echo sounder observations. *Annals of Glaciology*, 37:207–212.
- [Dahl-Jensen et al., 1997] Dahl-Jensen, D., Gundestrup, N. S., Keller, K., Johnsen, S. J., Gogineni, P., Allen, C. T., Chuah, T. S., Miller, H., Kipfstuhl, S., and Waddington, E. D. (1997). A search in north Greenland for a new ice-core drill site. *Journal of Glaciology*, 43(144):300–306.
- [Dahl-Jensen et al., 1993] Dahl-Jensen, D., Johnsen, S. J., Hammer, C. U., and Jouzel, J. (1993). Past accumulation rates derived from observed annual layers in the GRIP ice core from Summit, Central Greenland. In Peltier, W. R., editor, *NATO ASI Series, Vol. I, 12, Ice in the Climate System*, pages 517–532. Springer-Verlag, Berlin.
- [Dahl-Jensen et al., 1998] Dahl-Jensen, D., Mosegaard, K., Gundestrup, N., Clow, G. D., Johnsen, S. J., Hansen, A. W., and Balling, N. (1998). Past temperatures directly from the Greenland Ice Sheet. *Science*, 282:268–271.
- [Dansgaard, 1964] Dansgaard, W. (1964). Stable isotopes in precipitation. *Tellus*, 16(4):436–468.
- [Dansgaard and Johnsen, 1969] Dansgaard, W. and Johnsen, S. J. (1969). A flow model and a time scale for the ice core from Camp Century, Greenland. *Journal of Glaciology*, 8(53):215–223.
- [Evans, 1965] Evans, S. (1965). Dielectric properties of ice and snow – a review. *Journal of Glaciology*, 5(42):773–792.

- [Fahnestock et al., 2001] Fahnestock, M., Abdalati, W., Joughin, I., Brozena, J., and Gogineni, P. (2001). High geothermal heat flow, basal melt, and the origin of rapid ice flow in central Greenland. *Science*, 294:2338–2342.
- [Fairbanks, 1989] Fairbanks, R. G. (1989). A 17,000-year glacio-eustatic sea level record: influence of glacial melting rates on the Younger Dryas event and deep-ocean circulation. *Nature*, 342(6250):637–642.
- [Feller, 1970] Feller, W. (1970). *An Introduction to Probability Theory and Its Applications*. John Wiley.
- [Fujita and Mae, 1994] Fujita, S. and Mae, S. (1994). Causes and nature of ice-sheet radio-echo internal reflections estimated from the dielectric properties of ice. *Annals of Glaciology*, 20:80–86.
- [Fujita et al., 1999] Fujita, S., Maeno, H., Uratsuka, S., Furukawa, T., Mae, S., Fujii, Y., and Watanabe, O. (1999). Nature of radio echo layering in the Antarctic ice sheet detected by a two-frequency experiment. *Journal of Geophysical Research*, 104(B6):13013–13024.
- [Glen, 1955] Glen, J. W. (1955). The creep of polycrystalline ice. In *Proceedings of the Royal Society of London*, volume 228 of *series A*, pages 519–538.
- [Gogineni et al., 1998] Gogineni, S., Chuah, T., Allen, C., Jezek, K., and Moore, R. K. (1998). An improved coherent radar depth sounder. *Journal of Glaciology*, 44(148):659–669.
- [Gogineni et al., 2001] Gogineni, S., Tammana, D., Braaten, D., Leuschen, C., Akins, T., Legarsky, J., Kanagaratnam, P., Stiles, J., Allen, C., and Jezek, K. (2001). Coherent radar ice thickness measurements over the Greenland ice sheet. *Journal of Geophysical Research*, 106(D24):33761–33772.
- [Grinsted and Dahl-Jensen, 2002] Grinsted, A. and Dahl-Jensen, D. (2002). A Monte Carlo-tuned model of the flow in the NorthGRIP area. *Annals of Glaciology*, 35:527–530.
- [Gudmandsen, 1975] Gudmandsen, P. (1975). Layer echoes in polar ice sheets. *Journal of Glaciology*, 15(73):95–101.
- [Hammer, 1980] Hammer, C. U. (1980). Acidity of polar ice cores in relation to absolute dating, past vulcanism, and radio-echos. *Journal of Glaciology*, 25(93):359–372.
- [Harrison, 1973] Harrison, C. H. (1973). Radio echo sounding of horizontal layers in ice. *Journal of Glaciology*, 12(66):383–397.
- [Hempel et al., 2000] Hempel, L., Thyssen, F., Gundestrup, N., Clausen, H. B., and Miller, H. (2000). A comparison of radio-echo sounding data and electrical conductivity of the GRIP ice core. *Journal of Glaciology*, 46(154):369–374.
- [Hvidberg et al., 2002] Hvidberg, C. S., Keller, K., and Gundestrup, N. S. (2002). Mass balance and ice flow along the north-northwest ridge of the Greenland ice sheet at NorthGRIP. *Annals of Glaciology*, 35:521–526.

- [Johnsen et al., 1997] Johnsen, S. J., Clausen, H. B., Dansgaard, W., Gundestrup, N. S., Hammer, C. U., Andersen, U., Andersen, K. K., Hvidberg, C. S., Dahl-Jensen, D., Steffensen, J. P., Shoji, H., Sveinbjörnsdóttir, A. E., White, J., Jouzel, J., and Fisher, D. (1997). The  $\delta^{18}\text{O}$  record along the Greenland Ice Core Project deep ice core and the problem of possible Eemian climate instability. *Journal of Geophysical Research*, 102(C12):26397–26410.
- [Johnsen et al., 1995] Johnsen, S. J., Dahl-Jensen, D., Dansgaard, W., and Gundestrup, N. (1995). Greenland palaeotemperatures derived from GRIP bore hole temperature and ice core isotope profiles. *Tellus*, 47B:624–629.
- [Johnsen et al., 2001] Johnsen, S. J., Dahl-Jensen, D., Gundestrup, N., Steffensen, J. P., Clausen, H. B., Miller, H., Masson-Delmotte, V., Sveinbjörnsdóttir, A., and White, J. (2001). Oxygen isotope and palaeotemperature records from six Greenland ice-core stations: Camp Century, Dye-3, GRIP, GISP2, Renland and NorthGRIP. *Journal of Quaternary Science*, 16(4):299–307.
- [Johnsen et al., 1989] Johnsen, S. J., Dansgaard, W., and White, J. W. C. (1989). The origin of arctic precipitation under present and glacial conditions. *Tellus*, 41B(4):452–468.
- [Johnson, 1977] Johnson, A. F. (1977). Creep characterization of transversely-isotropic metallic materials. *J. Mech. Phys. Solids*, 25:117–126.
- [Kanagaratnam et al., 2001] Kanagaratnam, P., Gogineni, S. P., Gundestrup, N., and Larsen, L. (2001). High-resolution radar mapping of internal layers at the North Greenland Ice Core Project. *Journal of Geophysical Research*, 106(D24):33799–33811.
- [Letréguilly et al., 1991] Letréguilly, A., Reeh, N., and Huybrechts, P. (1991). The Greenland ice sheet through the last glacial-interglacial cycle. *Palaeogeography, Palaeoclimatology, Palaeoecology (Global and Planetary Change Section)*, 90(4):385–394.
- [Menke, 1989] Menke, W. (1989). *Geophysical Data Analysis: Discrete Inverse Theory*. Academic Press.
- [Millar, 1981] Millar, D. H. M. (1981). Radio-echo layering in polar ice sheets and past volcanic activity. *Nature*, 292(5822):441–443.
- [Mosegaard, 1998] Mosegaard, K. (1998). Resolution analysis of general inverse problems through inverse Monte Carlo sampling. *Inverse Problems*, 14:405–426.
- [Mosegaard and Tarantola, 1995] Mosegaard, K. and Tarantola, A. (1995). Monte Carlo sampling of solutions to inverse problems. *Journal of Geophysical Research*, 100(B7):12431–12447.
- [North Greenland Ice Core Project members, 2004] North Greenland Ice Core Project members (2004). High-resolution record of Northern Hemisphere climate extending into the last interglacial period. *Nature*, 431:147–151.
- [Paren and Robin, 1975] Paren, J. G. and Robin, G. d. Q. (1975). Internal reflections in polar ice sheets. *Journal of Glaciology*, 14(71):251–259.
- [Paterson, 1994] Paterson, W. S. B. (1994). *The Physics of Glaciers*. Pergamon Press, Oxford.

- 
- [Riishøjgaard, 1989] Riishøjgaard, L. P. (1989). En undersøgelse af interne lag i centralgrønlandske radioekkkodata. Master's thesis, Department of Geophysics, Niels Bohr Institute for Astronomy, Physics, and Geophysics, University of Copenhagen, Denmark.
- [Tarantola and Mosegaard, 2000] Tarantola, A. and Mosegaard, K. (2000). Mathematical basis for physical inference. *arXiv:math-ph/0009020 v1*, pages 1–24.
- [Tarantola and Valette, 1982] Tarantola, A. and Valette, B. (1982). Inverse problems=quest for information. *Journal of Geophysics*, 50(3):159–170.
- [University of Kansas, RSL] University of Kansas (RSL). <http://tornado.rsl.ku.edu/southern.html>.
- [Waelbroeck et al., 2002] Waelbroeck, C., Labeyrie, L., Michel, E., Duplessy, J. C., McManus, J. F., Lambeck, K., Balbon, E., and Labracherie, M. (2002). Sea-level and deep water temperature changes derived from benthic foraminifera isotopic records. *Quaternary Science Reviews*, 21:295–305.